

Reservoir Quality and Controlling Mechanism of the Upper Paleogene Fine-Grained Sandstones in Lacustrine Basin in the Hinterlands of Northern Qaidam Basin, NW China



Lei Gong^{1,2}, Xianzhi Gao^{*1,2}, Futao Qu^{1,2}, Yongshu Zhang³, Guangya Zhang⁴, Jun Zhu³

1. College of Geosciences, China University of Petroleum, Beijing 102249, China

2. State Key Laboratory of Petroleum Resources and Prospecting, China University of Petroleum, Beijing 102249, China

3. Exploration & Development Research Institute of Qinghai Oilfield Company, PetroChina, Dunhuang 736202, China

4. Research Institute of Petroleum Exploration & Development, PetroChina, Beijing 100083, China

 Lei Gong: <https://orcid.org/0000-0001-5986-9411>;  Xianzhi Gao: <https://orcid.org/0000-0002-2695-3737>

ABSTRACT: The Upper Paleogene lacustrine fine-grained sandstones in the hinterlands of the northern Qaidam Basin mainly contain two sweet spot intervals. Fracture/fault, microfacies, petrology, pore features, diagenesis, etc., were innovatively combined to confirm the controlling factors on the reservoir quality of shallow delta-lacustrine fine-grained sandstones. The diagenesis of the original lake/surface/meteoric freshwater and acidic fluids related to the faults and unconformity occurred in an open geochemical system. Comprehensive analysis shows that the Upper Paleogene fine-grained sandstones were primarily formed in the early diagenetic B substage to the middle diagenetic A substage. Reservoir quality was controlled by fault systems, microfacies, burial-thermal history, diagenesis, hydrocarbon charging events (HCE), and abnormally high pressure. Shallow and deep double fault systems are the pathways for fluid flow and hydrocarbon migration. Sandstones developed in the high energy settings such as overwater (ODC) and underwater distributary channels (UDC) provide the material foundation for reservoirs. Moderate burial depth (3 000–4 000 m), moderate geothermal field (2.7–3.2 °C/100 m), and late HCE (later than E₃) represent the important factors to protect and improve pore volume. Meteoric freshwater with high concentrations of CO₂ and organic acids from thermal decarboxylation are the main fluids leading to the dissolution and reformation of feldspar, rock fragments, calcite and anhydrite cements. Abnormally high pressure caused by the undercompaction in a large set of argillaceous rocks is the key to form high-quality reservoirs. Abnormal pressure zones reduced and inhibited the damage of compaction and quartz overgrowth to reservoir pores, allowing them to be better preserved. A reservoir quality evaluation model with bidirectional migration pathways, rich in clay minerals, poor in cements, superimposed dissolution and abnormally high pressure was proposed for the ODC/UDC fine-grained sandstones. This model will facilitate the future development of fine-grained sandstone reservoirs both in the Upper Paleogene of the Qaidam Basin and elsewhere.

KEY WORDS: sandstone, reservoir quality, diagenetic system, genetic mechanism, petroleum research, Upper Paleogene, northern Qaidam Basin.

0 INTRODUCTION

Worldwide hydrocarbon production is generally believed to be the main cause for the decline in oil and gas reserves in conventional sandstone and carbonate reservoirs (Zhang et al., 2018; Bentley, 2002). Unconventional reservoirs, especially lacustrine fine-grained clastic sedimentary rocks, have made key breakthroughs and have attracted more attention from geologists in recent years (Peng et al., 2022; Li et al., 2020; Wang J

et al., 2019; Zhang et al., 2019; Zhao et al., 2017; MacQuaker et al., 2014). The reservoir quality of fine-grained clastic sequences and its genetic mechanism have been extensively investigated (Wang F et al., 2021; Zhang and Li, 2018; Chen et al., 2016). For example, Zhang et al. (2021) divided two sets of high-quality Cenozoic reservoirs into ultralow poro-perm fine-grained clastic rocks of the Mangya area, western Qaidam Basin, and attributed their controlling factors to compaction, early calcite cementation and dissolution of shallow acidic fluids. Ye et al. (2021) analyzed thin-bedded fine-grained sandstones in the third and fifth members of the Xujiahe Formation in the western Sichuan depression and believed that the sweet spot reservoirs were the result of hydrocarbon generation, dissolution, and fracturing. Zhang P H et al. (2020) elucidated the genetic mechanism of oil-bearing fine-grained sandstones from

*Corresponding author: gaoxz@cup.edu.cn

© China University of Geosciences (Wuhan) and Springer-Verlag GmbH Germany, Part of Springer Nature 2023

Manuscript received December 17, 2021.

Manuscript accepted June 10, 2022.

the perspective of diagenetic controls on reservoir quality, such as compaction, cementation (kaolinite, pore-lining chlorite, calcite), and dissolution. Moreover, Pantopoulos et al. (2021), Pan Y S et al. (2021), and Wang et al. (2022) also noted the controlling mechanism of high-quality fine-grained sandstone reservoirs in lacustrine basins from the aspects of depositional conditions, pore structure, and pore fluid, respectively. Reservoir quality affects oil-gas exploration by controlling the flow, storage and distribution of fluids within fine-grained sandstones (Zhang X L et al., 2020). However, the quality is closely related to the complex pore structure and high heterogeneity of reservoir spaces and becomes difficult to predict (Cao et al., 2021; Pan Y S et al., 2021; Luo et al., 2019; Wang et al., 2017). Therefore, it is significant to evaluate and analyze the reservoir quality of fine-grained clastic rocks.

The Upper Paleogene fine-grained sandstone is one of the most important lacustrine reservoirs in the northern Qaidam Basin, NE Tibetan Plateau. Despite fine-grained sedimentary rocks and mid-deep burial depths (2 200–4 800 m), most Upper Paleogene reservoirs still possess preserved porosities of up to 15% and even *in situ* permeabilities of $10 \times 10^{-3} \mu\text{m}^2$. These space types, including intergranular pores and small amounts of dissolved pores, are the main basis for hydrocarbon accumulation (Liao et al., 2022). Interconnected fractures/faults affect the high quality and high yield of oil and gas exploitation (Wang J G et al., 2019). In addition, the Upper Paleogene sequences are characterized by well-developed fault systems connected with source rocks, basal unconformities and thin-bedded single sand bodies. These external conditions therefore have variable features, resulting in highly heterogeneous reservoir quality (Cao et al., 2021). Recent exploration (5 exploratory wells since 2018) in the hinterlands indicates the high production potentials for low permeability gas reservoirs in the delta-lacustrine fine-grained deposits. Although the Upper Paleogene sandstones in the northern Qaidam Basin have previously been studied on reservoir features, depositional settings and diagenesis (e.g., Wang Y T et al., 2021; Guo et al., 2018a; Ma et al., 2018), these studies largely focus on a single factor, as opposed to the effect of all factors on reservoir quality. Therefore, the complex genetic mechanism of high-quality gas reservoirs remains mysterious, which poses great challenges to oil-gas exploration. The issues must be solved to better understand the abdominal petroleum systems and promote oil-gas exploration and development in the northern Qaidam Basin.

Focusing on the Upper Paleogene abdominal fine-grained sandstones in the northern Qaidam Basin, this study was designed to investigate the origin and timing of dissolution associated with meteoric freshwater leaching and HCE. The pore space types, pore structure and properties in the sandstones changed during deposition and burial diagenesis, so studying the complex controlling factors of high-quality reservoirs is one of the main aims. Fracture/fault systems and pore water geochemistry are used to analyze the element sources of diagenetic minerals and to confirm the geochemical conditions of the diagenetic system. Additionally, this study also illustrates the diagenetic stage and sequence of Upper Paleogene fine-grained sandstones with petrological observation, clay mineral analysis, homogenization temperature (*HT*) of fluid inclusions and isoto-

pic analysis. A sandstone model of reservoir microfacies is described, which comprises variations in faults, burial-thermal history, diagenesis, HCE, and porosity evolution. This model, first applied to Upper Paleogene fine-grained sandstones, provided a basis for reservoir quality evaluation. The reservoir quality framework may also guide the resource exploration of lacustrine fine-grained sandstone reservoirs in other basins.

1 GEOLOGICAL SETTING

1.1 Qaidam Basin

The Qaidam Basin, situated in Qinghai Province, NW China (Fig. 1a), is a Meso-Cenozoic fault basin with a Precambrian metamorphic basement (Zhang X L et al., 2020). This intermontane lacustrine basin is now surrounded by three large mountains: the Qilian Mountains to the northeast, the Kunlun Mountains to the south, and the Altun Mountains to the northwest (Fig. 1b). According to the current topographic changes and recent data, the Qaidam Basin consists of four tectonic subunits, including the northern Qaidam depression, the eastern Qaidam depression, the western Qaidam depression, and the Altun piedmont slope (Fig. 1b) (Bao et al., 2017). The study area is located west of the northern Qaidam depression, which is divided into the Lenghu tectonic belt, the Eboliang tectonic belt, the Kuntayi depression, and part of the Yibei and Yahu depressions (Fig. 1b).

Geologic sections derived from seismic data indicate that there existed two series of fault systems, the shallow one and the deep one (Figs. 1c, 1d). Abundant anticlines and thick Neogene-Quaternary sediments developed within the scope of the shallow fault system, resulting in a relatively broken ridge structure. A deep fault system controlled the deposition of the Upper Paleogene strata (Fig. 1c) (Guo et al., 2017). The northern Qaidam Basin was intricately revised and integrated from northeast to southwest under the joint action of the Qilian Mountains fold-thrust and the Altun Mountains left-lateral strike-slip fault. As a result, two rows of anti-S-shaped NW-SE-trending fault-fold corridor areas and thin sedimentary features in the NE and thick features in the SW were formed (Fig. 1d) (Zhang et al., 2018; Yin and Harrison, 2000).

1.2 Stratigraphy

The Paleogene contains the Lulehe (E_{1+2}), Xiaganchaigou (E_3) and Shangganchaigou (N_1) formations (Fms) (Fig. 2). The Qaidam Block was uplifted and denuded by tectonic compression during the Late Jurassic–Late Cretaceous, resulting in a regional unconformity between E_{1+2} and the Lower Jurassic in the study area (Fig. 2) (Ren et al., 2019). The Upper Paleogene, composed of E_3 and N_1 with a mean depth of 2 200–4 200 m, was deposited in the Late Eocene–Oligocene fan-fluvial-delta-lake system (Zou et al., 2015). E_3 comprises the lower member (E_3^1) and the upper member (E_3^2). The lacustrine basin area expanded with the decrease in the braided river delta, and the water deepened obviously, but eventually all reduced slightly during the Late Paleogene (Song et al., 2013). The paleoclimate became colder and drier but ended up relatively warm and humid (Fig. 2) (Guo P et al., 2018).

1.3 Features of Source Rocks

The Upper Paleogene oil and gas in the northern Qaidam

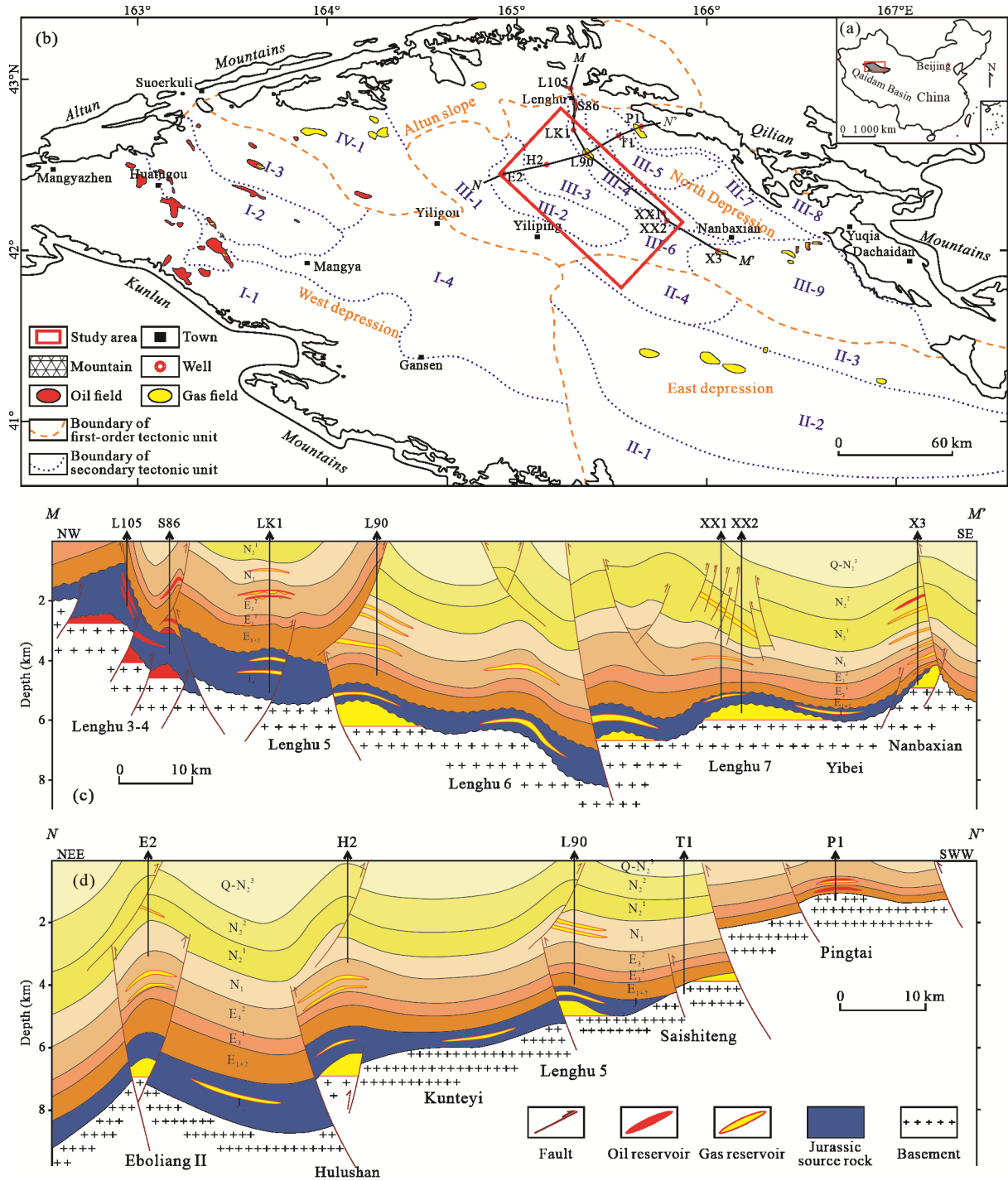


Figure 1. Maps revealing (a) the location of Qaidam Basin in NW China; (b) the location of hinterlands in the northern Qaidam Basin as the study area; (c) NW-SE-trending through-well geologic section; and (d) SW-NE-trending through-well geologic section. Secondary tectonic unit: I-1. southwest slope; I-2. Yingxiongling tectonic belt; I-3. northwest tectonic belt; I-4. Mangdong tectonic belt; II-1. south slope; II-2. central depression; II-3. north slope; II-4. Yahu depression; III-1. Yiliping depression; III-2. Eboliang tectonic belt; III-3. Kuntayi depression; III-4. Lenghu tectonic belt; III-5. Qianfu tectonic belt; III-6. Yibei depression; III-7. Saishiteng depression; III-8. Qilian piedmont belt; III-9. Mahai uplift; IV-1. Dafengshan uplift.

Basin came from the Lower Jurassic Huxishan Formation (Fm) (J_1h), Xiaomeigou Fm (J_1x), and the first to the third members of Dameigou Fm (J_1d^{1-3}) source rocks (Fig. 1c) (Ma et al., 2018; Liu et al., 2017). The J_1h source rocks with a single thickness of 0.5–31.5 m comprise dark gray mudstones, silty mudstone, siltstones, calcareous mudstone and coal seams. The J_1x source rocks with a single thickness of 0.2–27.3 m are composed of dark

gray mudstones, calcareous mudstone and thin seams. The J_1d^{1-3} source rocks with a single thickness of 0.2–19.9 m consist of black brown oil shale, black, dark gray mudstones, shales, siltstones, calcareous mudstone and coal seams (Ma et al., 2018). With the Middle Jurassic–Cretaceous hiatus caused by tectonic uplift, the source rocks of these formations began to generate hydrocarbons abundantly in the Late Eocene (Ma et al., 2018).

2 DATASETS, SAMPLES AND METHODS

The datasets used, such as conventional cores, well logs, physical properties, seismic sections, *HT* of inclusions, and formation water geochemistry, were all obtained from the Exploration & Development Research Institute, Qinghai Oilfield Company. In addition, Petromod software was used to restore and reconstruct the burial history on the basis of previous research at this institute. Then, the thermal history was calculated from the current geothermal gradient and burial history.

The sedimentary study of Upper Paleogene sandy rocks in the hinterlands of the northern Qaidam Basin was carried out in association with well and core data. More than 20 Upper Paleogene wells were surveyed with core and logging data. Indicators (e.g., rock color, lithology, texture, structure) in cores were observed to analyze the sedimentary system. The facies distribution of the Upper Paleogene basin was clarified by using single-well coring columns showing the vertical developments of braided river delta and lake facies. Seismic interpretation was targeted particularly to reveal and trace the fault systems and contact relationships of the Upper Paleogene and overlying/underlying strata. A total of 2 3D seismic blocks and 30 2D seismic lines were interpreted during this analysis.

Twenty-three mudstone samples and 40 sandstone samples were selected from the E_3 (18 samples) and N_1 (45 samples) cores (~179 m) of 14 key wells. Petromineralogy and pore type analyses of 26 thin sections impregnated with blue epoxy resin were performed by a 300-point counting Zeiss Axio Imager A1/A2 polarizing microscope. Petrology and areal porosity data are accurate to one decimal place. Twenty-one sandstone samples were used for grain-size analysis by measuring the spatial (angular) distribution of diffracted/scattered light energy under an MS-2000 laser grain size analyzer (LGSA) to define microfacies and the environment. Thirty-three core samples were drilled into plunger plates with a length of 2.5 cm and diameter of 2.5 cm, placed into a mixed solution of alcohol and benzene for the extraction experiment, and dried at 50 °C for 24 h. After that, conventional permeability and porosity measurements were conducted on sandstone samples using DX-07G permeability and Ultra Pore-400 porosity measuring instruments to facilitate their physical property analysis. However, the data used in this study were not derived entirely from this method but partly from nuclear magnetic resonance (NMR) analysis under a RecCore-3010 NMR core analyzer. Based on the above, ~370 physical property data were selected in the depth range of 1 000–6 200 m. Poro-perm analyses are accurate to one decimal place.

More than 26 samples were successively coated with gold film, sprayed with carbon and inspected by a Zeiss EVO-18 scanning electron microscope (SEM) to observe authigenic minerals, pore geometry and cements in sandstones. The capillary pressure curve, pore structure parameters and pore-throat radius distribution of 72 core samples were obtained by high-pressure mercury injection. The AutoPore IV 9520 automated mercury porosimeter possessed a maximum experimental pressure of 241 MPa, and the specific testing conditions were as follows: temperature 25 °C, relative humidity 45%, surface tension 0.48 N/m, and wetting contact angle 140°. X-ray diffraction (XRD) whole rock and clay mineral analyses of 18 samples identified the type and content of minerals and grains and

confirmed the modal composition by a PANalytical Empyrean X-ray diffractometer at a temperature of 23 °C and a relative humidity of 50%. Whole rock and pore water geochemistry analysis is accurate to one decimal place, whereas clay mineral analysis is accurate to whole numbers. Five samples were analyzed by fluorescence microscopy, and HCE was investigated in combination with fluid inclusion temperatures.

3 RESULTS

3.1 Fracture/Fault Systems

The fractures/faults in the study area run through the whole Paleogene, some even into the Jurassic or Cretaceous (Figs. 2 and S1A). Multiple fractures/faults are developed throughout the Upper Paleogene, some of which are deep and cut through the major source rocks and the strata (Fig. S1A). Four deep faults cover most of the well and 2D seismic regions (Fig. S1B). In general, the fracture/fault zones are composed of nearly 15 faults with lengths of 10–25 km, extending more than 40 km in parallel arrangement (Fig. S1B).

3.2 Sedimentary Facies Distribution

E_3^1 was deposited in a large-scale braided river delta plain, delta front and small-scale shore-shallow lake (Figs. S2A, S2D). The shallow delta plain consists of ODC and natural barrier microfacies (Fig. S2A). Then, E_3^2 mainly developed a braided river delta front and shore-shallow lake (Figs. S2B, S2E). The shallow delta front mainly comprises UDC, interdistributary bay and mouth bar microfacies (Fig. S2B). During the deposition of N_1 , the setting was composed of a large-scale shore-shallow lake and a small-scale delta front (Figs. S2C, S2F). Beach bars and sandflats are crucial sandstones in shore and shallow lake deposits (Fig. S2C).

3.3 Petrology of Fine-Grained Sandstones

The Upper Paleogene sandstones are dominated by feldspathic litharenite and lithic arkose. However, the petrological features of different tectonic belts are not exactly the same, averaged as Lenghu No. 5 $Q_{33.1}F_{36.2}R_{30.7}$, Lenghu No. 6 $Q_{38.8}F_{33.5}R_{27.7}$, Lenghu No. 7 $Q_{34.8}F_{33.1}R_{32.1}$, Hulushan $Q_{40.4}F_{50.8}R_{8.8}$, Eboliang $Q_{28.3}F_{23.3}R_{48.4}$, Yahu $Q_{20.5}F_{31.2}R_{48.3}$ (Fig. 3a). The fine-grained sandstones in terms of grain size are divided into medium-fine sandstone (Figs. 4a, 4e), fine sandstone (Figs. 4b, 4f), siltstone (Figs. 4c, 4g) and argillaceous siltstone (Figs. 4d, 4h). They are cemented by calcite, ferrocalcite and anhydrite (Figs. 4i, 4j, 4n, 4p). The clastic composition is dominated by highly weathered feldspar (K-feldspar and albite), accounting for ~35.0% of the clastic grain volume (Figs. 4k, 4n, 4o, 4p, Table S1). Lithic grains, which represent 32.1% of the clastic grain volume, are composed of metamorphic (quartzite, phyllite and slate), minor volcanic (monzonite and arkosite), and sedimentary rock fragments (Figs. 4k–4p and Table S1). The grains are moderately to well sorted, subangular to subrounded, fine and silty grained with few medium and argillaceous grains (Figs. 4i–4p).

In addition, little difference in petrological features occurs between microfacies. The clastic grains consist of 28.0%–33.5% quartz, 35.9%–37.2% feldspar, 22.1%–23.8% metamorphic, 5.5%–11.0% volcanic, and 0.0%–4.3% sedimentary rock fragments (Table 1).

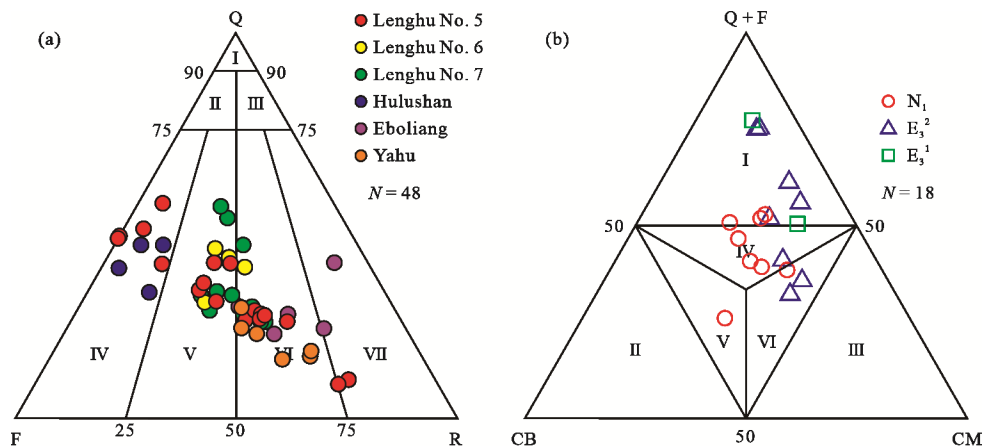
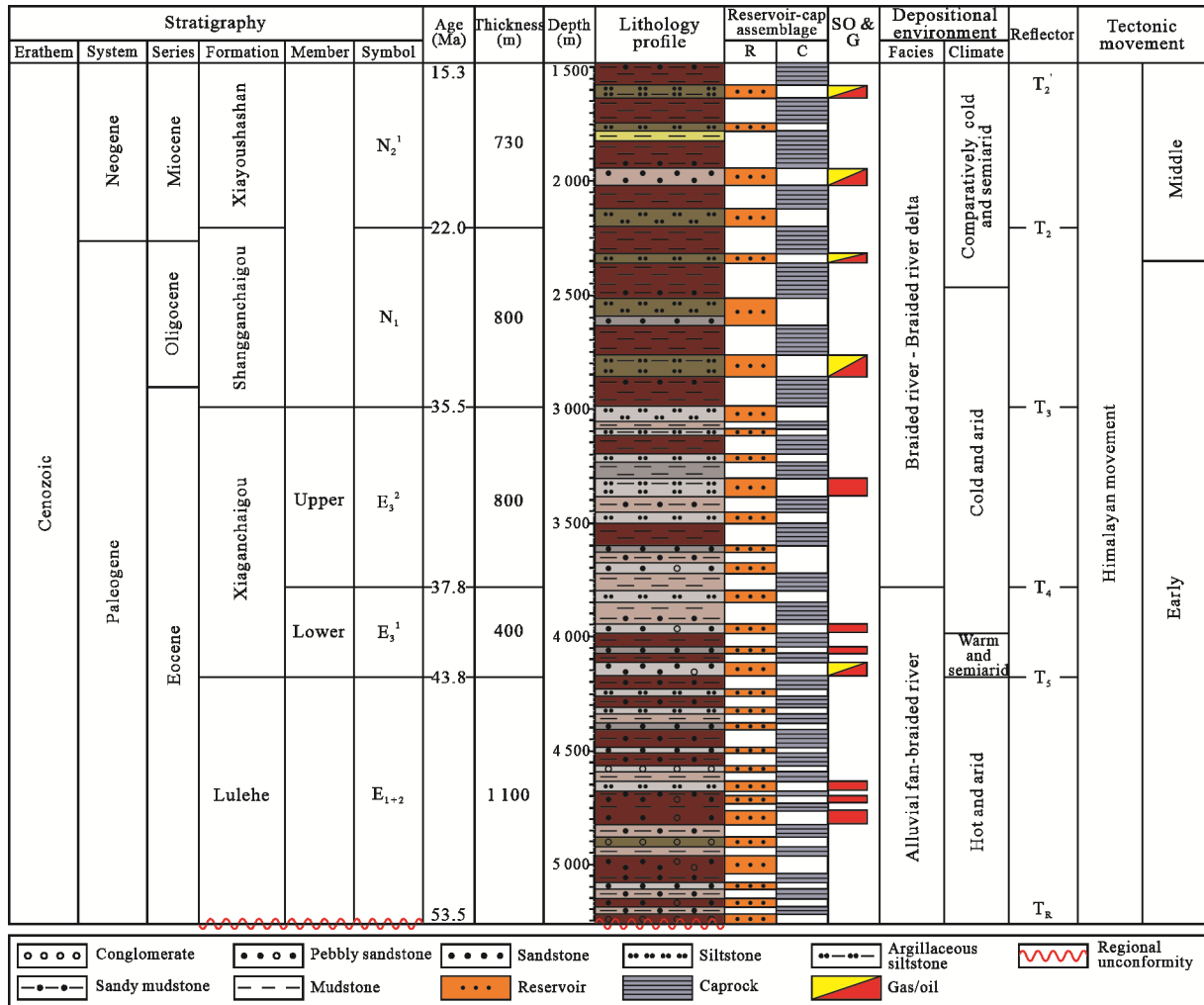


Figure 3. Petrological (a) and mineralogical (b) triangular diagrams reflecting the composition and classification of the Upper Paleogene sandstones in the study area (modified after Folk, 1980 and Peng et al., 2022). Q. Quartz; F. feldspar; R. rock fragments; I. quartz arenite; II. Subfeldsarenite; III. Sublitharenite; IV. Arkose; V. lithic arkose; VI. feldspathic litharenite; VII. Litharenite; Q + F. quartz and feldspar; CB. carbonate minerals; CM. clay minerals; I. felsic fine-grained rock; II. carbonate rock; III. clay rock; IV. felsic mixed fine-grained rock; V. carbonate mixed fine-grained rock; VI. clayey mixed fine-grained rock.

3.4 Mineralogy of Fine-Grained Sandstones

Authigenic minerals are mostly composed of quartz, feldspar, carbonate, sulfate (anhydrite and barite), silicate (analcite

and laumontite) and clay minerals (Table S2). These minerals have high contents of clay minerals, containing illite (45.6%), an I/S mixed layer (31.8%), chlorite (15.1%), smectite (6.4%)

Table 1 Petrology of major microfacies sandstones in the study area. Note that all data are average values

Microfacies sandstones	Quartz (%)	Feldspar (%)	Brittle grains (quartz + feldspar) (%)	Rock fragments (%)		
				Metamorphic	Volcanic	Sedimentary
Beach bar	32.8	35.9	68.7	23.7	5.5	2.1
Beach bar/underwater distributary channel	31.8	13.1	44.9	36.1	15.7	3.3
Underwater distributary channel	33.5	36.0	69.5	23.2	6.0	1.3
Mouth bar	28.0	37.2	65.2	23.8	11.0	0.0
Overwater distributary channel	29.9	36.4	66.3	22.1	7.3	4.3
Upper Paleogene	31.2	31.7	62.9	25.8	9.1	2.2

and a minor C/S mixed layer (Fig. 3b, Table S3). The carbonate, as the principal cement, consists of calcite and lesser dolomite, with contents of 8%–42%, 18.5% (XRD analysis) and 14.4% (thin-section observation) on average (Fig. 3b, Table S2).

Sparry calcite revealed clear epochal phenomena and was formed in early and late generations. The early generation is a tightly interlocking mosaic of calcite crystals, while the late generation is characterized by isolated rhombs or partial grain replacements, such as ferrocalcite. Iron-free calcite cements partially or completely block the intergranular pores (Fig. 5). In the total calcite cements, the early cements (avg. 93%) are superior to the late ones (avg. 7%). Anhydrite cements, ranging from 0 to 7.2% (avg. 2.0%), occur occasionally in argillaceous siltstones (Table S2, Figs. 4j, 4n). In addition, the anhydrite cements were dissolved and metasomatized by calcite, usually in a calcite-like form for two generations. Chlorite cements are present as rims and surrounded by calcite, quartz and anhydrite (Fig. 5). Then, some albite forms pore-filling chlorite. Quartz overgrowth occurs around feldspar or quartz surrounded by calcite grains. Feldspar overgrowth is often surrounded by calcite cements and develops only in some areas (e.g., Eboliang).

3.5 Pore Spaces, Pore Structure and Physical Properties

The pore types of the Upper Paleogene fine-grained sandstones consist of major primary pores, secondary pores (intra-granular and intergranular dissolved pores) and few microfractures (Figs. 5 and 8). Triangular or polygonal primary pores with regular edges are larger than intergranular dissolved pores and are associated with chlorite rims (Figs. 5a, 5d, 5e, 5l). Intergranular pores contain major residual primary pores and minor amounts of dissolved pores (Figs. 5 and 6).

The total areal porosity, including primary pores (3.03%), secondary pores (1.24%), and microfractures (0.15%), decreases rapidly with depth in the range of 1 000–3 000 m and slightly below 3 000 m (Figs. 6a, 6b). The variation trend of the N_1 areal porosity with depth is basically equivalent to that of the whole strata (Fig. 6b). In contrast, the trend of the total areal porosity in E_3 generally increases with depth. In addition, the total areal porosity in the same tectonic belt is characterized by a wide distribution (Fig. 6b). The absolute and relative porosities of residual primary pores, mainly occurring between 1 000 and 3 500 m, decrease rapidly with depth as a whole but increase slowly in some places (3 500–5 000 m in absolute porosity and 1 000–2 000 m in relative porosity) (Figs. 6c, 6f). Dissolved pores were observed in the lower part (3 200–5 000 m), but a relative minority are observed in the upper part (Fig. 6d).

The absolute porosity slightly decreases but increases between 2 600 and 3 200 m (Fig. 6d). The relative porosity slightly decreases or hardly increases above 2 400 and below 4 000 m but rapidly increases between 2 400 and 4 000 m (Fig. 6g). The absolute and relative porosities of microfractures hardly decrease in the whole section, whereas they first increase and then decrease between 2 500 and 4 000 m (Figs. 6e, 6h).

The results of the mercury ejection curve show that the distribution of residual mercury saturation ranges from 43.02% to 74.82%, with an average of 57.74%. The ejection saturation was between 15.15% and 26.54%, with an average of 18.89% (Fig. S3A). Generally, there is one main peak in the pore-throat radius distribution of high porosity/permeability cores, but only the lowest porosity/permeability cores present a double peak phenomenon. The distribution range of the left peak is 0.004–0.690 μm (avg. 0.329 μm). The distribution range of the right peak is 19.683–23.732 μm (avg. 21.708 μm) (Fig. S3B). Pore structure parameters such as the displacement pressure ($R = 0.69$) and the max throat radius ($R = 0.69$) are well correlated with core permeability (Fig. S4). There exists a positive correlation between the maximum mercury saturation or average pore-throat radius and core permeability, although the coefficient is not very high (Fig. S4).

The core porosity, ranging from 2% to 23% (avg. 8.68%), decreases with burial depth on the whole but increases slightly from 2 300 to 3 100 m and 3 600 to 4 000 m (Fig. S5A). The core permeability varies approximately between 0.01×10^{-3} and $10 \times 10^{-3} \mu\text{m}^2$ with an average of $0.74 \times 10^{-3} \mu\text{m}^2$ and is similar to the trend of porosity but increases in the range of 2 100–2 900 and 3 500–4 000 m and hardly decreases at the base (Fig. S5B).

3.6 Burial-Thermal History and Pore Water Geochemistry

Burial and thermal histories vary in different tectonic belts (Fig. S6). The sandstones are characterized by shallow burial depths (0–1 800 m) and moderate geothermal fields (2.7–2.9 $^{\circ}\text{C}/100 \text{ m}$) in the Lenghu tectonic belt, large depths (0–6 000 m) and moderate geothermal fields (2.8–2.9 $^{\circ}\text{C}/100 \text{ m}$) in the Kuntayi depression, and rapid burial depths (>7 000 m) and high geothermal fields (3.1–3.2 $^{\circ}\text{C}/100 \text{ m}$) in the Eboliang and Yahu tectonic belts (Fig. S6). The burial depth of the J_2 source rocks can even reach 6 000–8 000 m with the current high-geotemperature of 135–175 $^{\circ}\text{C}$ (Figs. S6 and S7).

Pore waters consist of major CaCl_2 water and minor Na_2SO_4 water and MgCl_2 water (Table S4). These waters are generally weakly acidic, with pH values ranging from 5.7 to 7.0 (Table S4). Salinity varies widely from 726.6 to 116 464.5

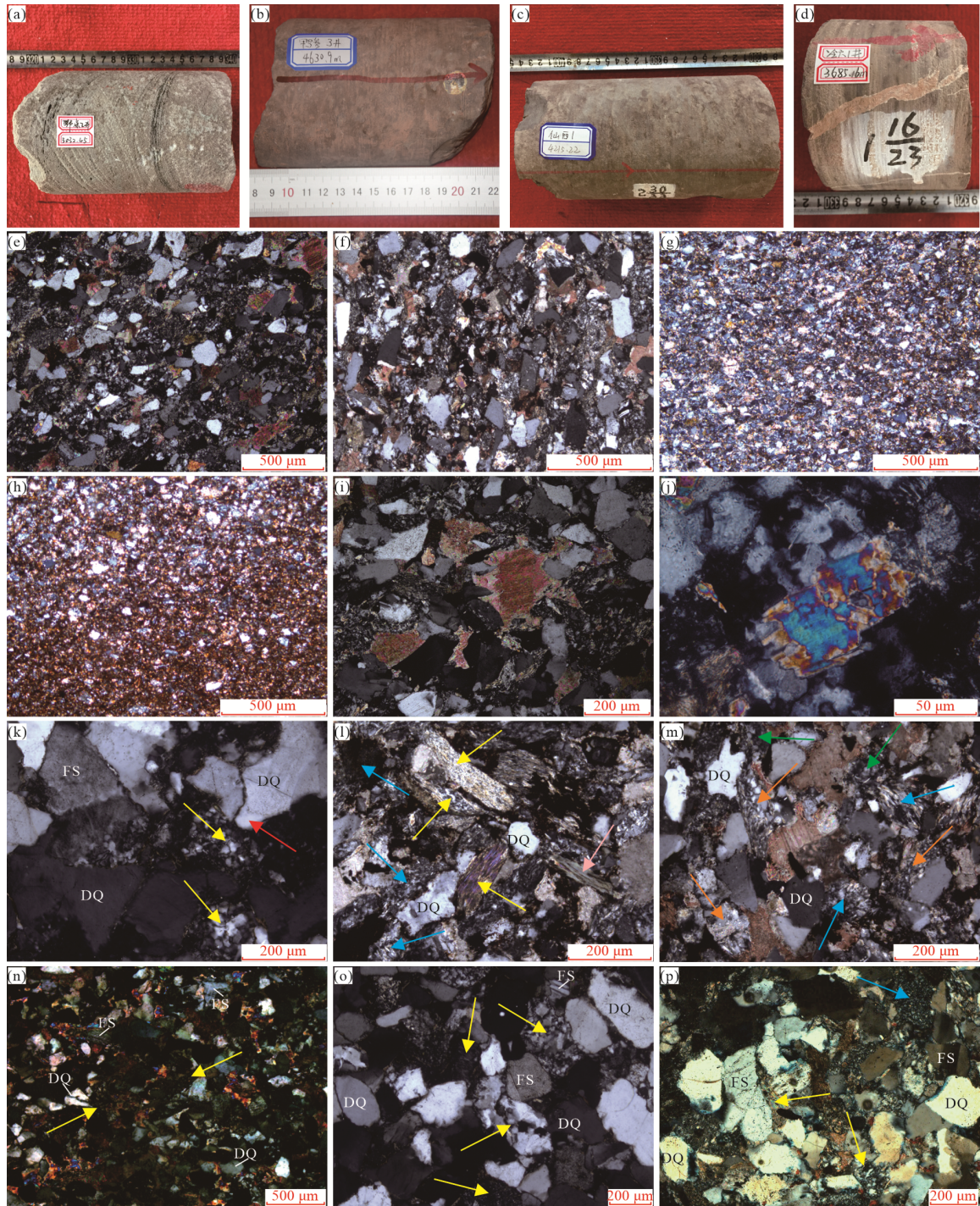


Figure 4. Petrology and mineralogy of the Upper Paleogene fine-grained sandstones (all micrographs taken under cross-polarized light), Q: quartz; F: feldspar. (a) Core photograph (CP) of medium-fine sandstone with cross-bedding, well ES2, 3 032.45 m, N_1 . (b) CP of fine sandstone with parallel bedding, well YC3, 4 630.90 m, N_1 . (c) CP of siltstone with oblique bedding, well XX1, 4 215.22 m, E_3^2 . (d) CP of argillaceous siltstone interbedded with fine sandstone, and developed high-angle fracture filled by calcite vein, well LL1, 3 685.16 m, E_3^2 . (e) Thin-section micrograph (TSM) of medium-fine feldspathic litharenite, well ES2, 3 032.45 m, N_1 . (f) TSM of fine feldspathic litharenite, well YC3, 4 630.90 m, N_1 . (g) TSM of silty lithic arkose, well XX1, 4 215.22 m, E_3^2 . (h) TSM of argillaceous lithic arkose, well LL1, 3 685.16 m, E_3^2 . (i) TSM revealing calcite characterized by porous cementation, well ES2, 3 032.40 m, N_1 . (j) TSM revealing pore-filling anhydrite and replacing the mineral, well ES2, 3 032.40 m, N_1 . (k) TSM revealing metamorphic rock fragment (MF) (quartzite, yellow arrow), quartz overgrowth (red arrow) and feldspar, well XX1, 4 852.45 m, E_3^1 . (l) TSM revealing MF (quartzite, phyllite and schist, yellow arrow), volcanic rock fragment (VF) (andesite, basalt and tuff, cyan arrow) and chlorite (pink arrow), well YC3, 4 630.90 m, N_1 . (m) TSM revealing calcite cement, high-grade (orange arrow) and low-grade (green arrow) MF, and VF (cyan arrow), well YC3, 4 630.90 m, N_1 . (n) TSM revealing quartz, feldspar, MF (quartzite, yellow arrow), calcite and anhydrite cements, well LL1, 3 680.58 m, E_3^2 . (o) TSM revealing MF (quartzite and schist, yellow arrow), quartz and feldspar, well XX1, 4 852.45 m, E_3^1 . (p) TSM revealing quartz with wavy extinction, feldspar with kaolinization or sericitization, MF (quartzite and phyllite, yellow arrow), VF (arkosite, cyan arrow), calcite and ferrocalcite cements, well XX1, 4 115.06 m, E_3^2 .

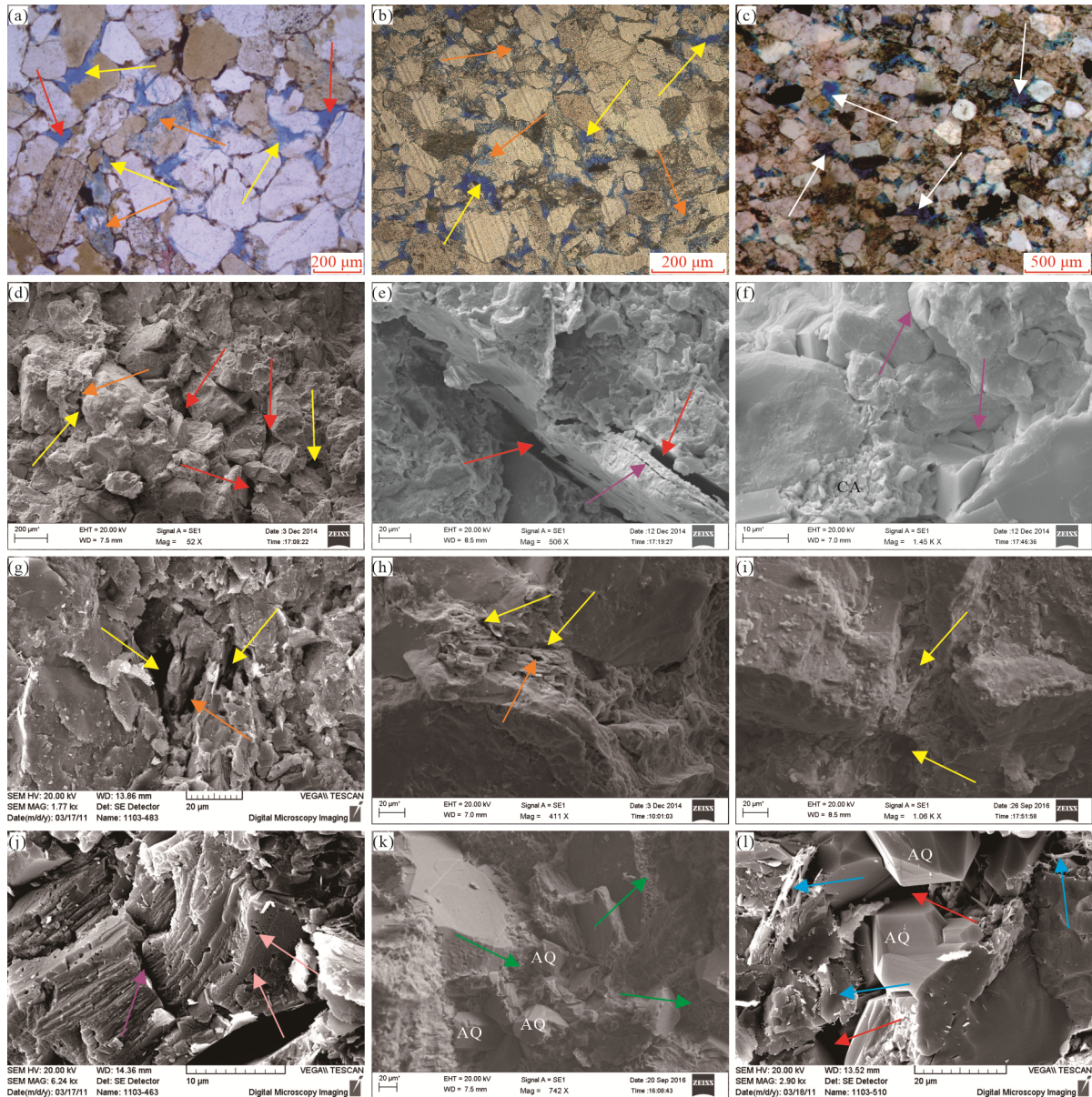


Figure 5. Pore space types and features of the Upper Paleogene fine-grained sandstones (all micrographs under plane-polarized light taken), AQ. Authigenic quartz; CA. calcite cement. (a) Casting thin-section micrograph (CTM) revealing residual primary pores (RP, red arrow), intergranular dissolved pores (EP, yellow arrow) and intragranular dissolved pores (AP, orange arrow), well XX1, 4 852.45 m, E_3^1 . (b) CTM revealing EP (yellow arrow) and AP (orange arrow), well ES2, 3 032.40 m, N_1 . (c) CTM revealing complex pores (white arrow) formed by the connection between RP and EP, pore-filling calcite cement, well LL1, 3 680.58 m, E_3^2 . (d) SEM image revealing RP (red arrow), EP (yellow arrow) and AP (orange arrow), well Y2, 1 422.82 m, E_3^2 . (e) SEM image revealing RP (red arrow) and hydromica with microfractures (purple arrow), well LX1, 1 048.37 m, N_1 . (f) SEM image revealing pore-filling calcite cement and grain edge microfractures (purple arrow), well LX1, 1 049.27 m, N_1 . (g) SEM image revealing EP (yellow arrow) and AP (orange arrow) formed by K-feldspar dissolution, well ES1, 3 994.52 m, N_1 . (h) SEM image revealing EP (yellow arrow) and AP (orange arrow) formed by calcite cement dissolution, well Y2, 1 213.99 m, E_3^2 . (i) SEM image revealing EP (yellow arrow) with pathway taken by acidic fluids, well XX1, 4 850.80 m, E_3^1 . (j) SEM image revealing micropores (pink arrow) and microfractures (purple arrow) in calcite grains, well ES1, 3 989.64 m, N_1 . (k) SEM image revealing chlorite rims (green arrow) closely bonded to grain surface and formed prior to authigenic quartz, well XX1, 4 214.52 m, E_3^2 . (l) SEM image revealing RP (red arrow) filled with authigenic quartz and illite (cyan arrow), well ES1, 3 997.12 m, N_1 .

mg/L (avg. 38 797.4 mg/L) (Table S4). The ion concentrations and total salinity from J_1x to N_2^1 change slightly in the vertical section but obviously in the lateral direction (Fig. 7). In addition, the vertical variation range of the Lenghu No. 5 and No. 7 tectonic belts is small and slightly reduced. The pore waters in the Eboliang, Yahu, and Hulushan tectonic belts increase signif-

icantly with depth and present obvious lateral differences (Fig. 7).

3.7 Fluorescent Display and Temperature of Fluid Inclusions

Microscopically, the organic inclusions show yellow-

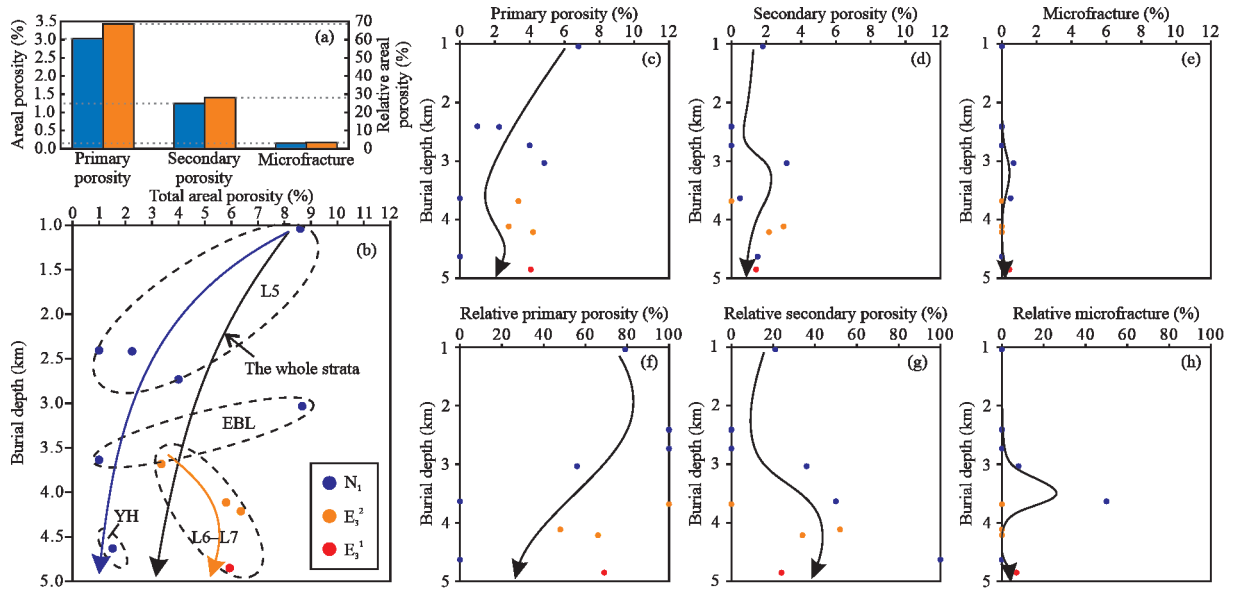


Figure 6. Vertical distribution of pores in the Upper Paleogene fine-grained sandstones. L5. Lenghu No. 5 tectonic belt; L6–L7. Lenghu No. 6 and No. 7 tectonic belts; EBL. Eboaliang tectonic belt; YH. Yahu depression. Porosity, the percentage of pore spaces in total rock volume; relative porosity, the relative percentage of specific pore in total pore spaces.

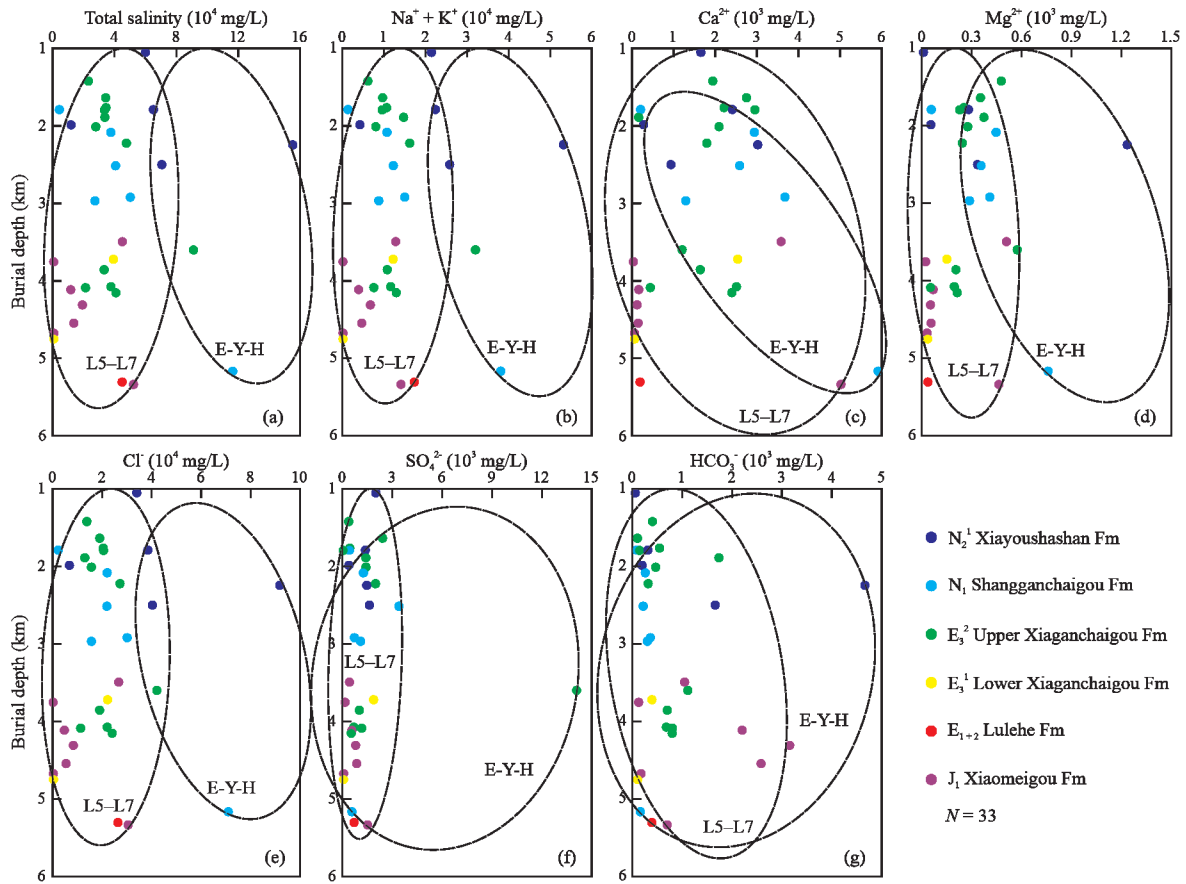


Figure 7. Vertical distribution of pore water geochemistry of the Paleogene and its adjacent strata. L5–L7. Lenghu No. 5 and No. 7 tectonic belts; E-Y-H. Eboaliang tectonic belt, Yahu depression, and Hulushan tectonic belt.

green or blue-white low-medium fluorescence. However, no fluorescence was observed in brine inclusions. The Upper Paleogene sandstones have yellow-green and blue-white fluorescent asphalt displays (Figs. S7A–S7D). In addition, the *HT* of

fluid inclusions is positively correlated with salinity (Fig. S7E). The linear features have a certain relevance with the burial depth of the samples: 4 data ($\omega(\text{NaCl}) > 7\%$) from below 3 400 m, while 5 data ($\omega(\text{NaCl}) < 5\%$) from above 2 850 m.

The *HT* values of brine inclusions in the Lenghu area are concentrated in the range of 60–130 °C and are higher than those of organic inclusions (50–100 °C) (Fig. S7F). The *HT* of brine inclusions with associated organic inclusions in the Eboliang area ranges of 80–104 °C and 112–136 °C (Fig. S7G). A brine inclusion was found at 3 991.2 m in well ES1, which had a high methane content and *HT* of 175 °C (Figs. S7G, S7H).

4 DISCUSSION

4.1 Micropore Structure for Reservoirs

Both residual mercury saturation and ejection saturation vary widely, which indicates that the pore and throat development of different cores are greatly different (Fig. S3B) (Yan et al., 2018; Wardlaw and Taylor, 1976). The peak distribution of the pore throats in different cores showed obvious polarization. The larger the peak radius was, the higher the peak ratio was, with overall increasing trend. The right peak was completely separated from the left peak. Both the span and radius of the right peak are relatively close, and the value ratio of the left peak was far greater than that of the right peak. The comparison indicates that the pore-throat development varies considerably on a small scale but is similar on a large scale, revealing unique attributes in the study area.

Pore structure parameters can describe the seepage capacity of the reservoirs. The parameters are closely related to the relative permeability curve and are mainly dominated by rock wettability but have little effect on porosity (Cao et al., 2015). The average pore-throat radius and max throat radius are both positively correlated with permeability, but the latter reveals a better correlation (Zhu et al., 2020; Cao et al., 2015). The small throats with larger volume ratios determine the average pore-throat radius, which reveals that the seepage capacity is mostly controlled by the development degree (ratio, radius) of the small-scale pore throats. For fine-grained sandstones, however, the maximum throat radius reflects the upper limit of the connected pore-throat volume, which can better represent the physical properties (Zhu et al., 2020). Therefore, the diversity of the throat distribution is the fundamental factor that causes the difference in seepage capacity of the fine-grained sandstones. The finer the reservoir is, the more contribution the throat makes to the effective spaces. Through the correlation analysis of parameters and permeability (Fig. S4), the pore structure has relatively strong heterogeneity in general. It reflects the features of “small pore-throat, poor sorting, high displacement pressure and poor pore-throat connectivity”.

The overall physical properties decrease gradually with depth (Fig. S5). The strata above 1 500 m are mainly high-quality reservoirs, with a maximum porosity and permeability of 30% and $300 \times 10^{-3} \mu\text{m}^2$, respectively. In addition to the top reservoirs, there are also two unusually excellent reservoirs at 3 000 and 4 000 m, which are in the moderately to deeply buried strata. The max porosity and permeability are close to 20% and $200 \times 10^{-3} \mu\text{m}^2$, respectively.

Thin-section observations for these two high-quality reservoirs confirmed that porosity is related to dissolution. Intra-granular dissolved pores are carved from feldspar and rock fragments reacting with acids (Figs. 5a, 5b, 5g). Unstable materials dissolve to form intergranular dissolved pores (Figs. 5a–

5i). All patterns imply the dissolved influences of acidic fluids associated with hydrocarbons (Feng et al., 2013). In addition to increasing physical properties, deep burial dissolution also increases the seepage systems related to structural fractures, thus enhancing reservoir performance (Jin et al., 2009). Apparent dissolution was detected in microscopic examinations, indicating that the properties were considerably improved. However, Guo J J et al. (2018) argued that the abrupt increase in these two ranges, especially at 4 000 m, was due to abnormally high pressure caused by the undercompaction of thin-bedded sandstone reservoirs developed in a large set of argillaceous rocks.

4.2 Diagenetic System of Fine-Grained Sandstones

4.2.1 Genesis of pore waters

The pore waters of depositional basins, originating from lake/sea water, absorbed water, meteoric water, interlayer water and thermal fluids, possess the potential to transport materials by solution (El-Ghali et al., 2006; Bjørlykke, 1993). The fluid evolution and carbon/oxygen isotopes of Paleogene carbonate rocks and cements show that the pore fluids were derived from organic acids supplied by underlying source rocks, original lake water, river/delta surface water, and meteoric water (Li et al., 2017; Yuan J Y et al., 2015). Extensive deep faults associated with uplift formed by basal unconformity connect source rocks to the Paleogene and offer crucial pathways for acid flow (Yuan et al., 2015a). Surface/meteoric water is able to penetrate ~2 km underground, showing the possibility of deep penetration (Gluyas et al., 1997a; Harrison and Summa, 1991). Pore waters comprise CaCl_2 water and minor Na_2SO_4 water with moderate salinity, which suggests that the waters are concerned with surface/meteoric freshwater leaching from shallow faults (Luo et al., 2019). It is noteworthy that the presence of MgCl_2 water in the pore waters is related to lake salinization rather than marine origin (Table S4). Therefore, the pore waters mainly came from organic acids, lake water and surface/meteoric water. A few waters were derived from the interlayer water expelled by smectite illitization (Du et al., 2021, 2019; Cai et al., 2018; Bethke and Altaner, 1986; Hower et al., 1976). Slight vertical variations in ion concentrations and total salinity provide evidence for relatively adequate mixing of pore waters of different origins (Bjørlykke and Gran, 1994).

4.2.2 Hydrocarbon charging order and time

The burial-thermal history, fluorescent display, *HT* and comprehensive features of source rocks can be interpreted to indicate that the sandstones received two periods of HCE, but the times of different tectonic belts had differences (Lai et al., 2017; Maast et al., 2011). The first charging event occurred between 32 and 22 Ma, and the second occurred between 9 and 4 Ma in Lenghu. The first charging event occurred from 14 to 8 Ma, and the second occurred from 7 to 3 Ma in Eboliang (Figs. S6, S7 and 8) (Fu et al., 2015).

With increasing depth and pressure, temperature and salinity also gradually increase, indicating that temperature/pressure is positively correlated with the intensity of the water-rock reaction. High-temperature and high-pressure fluids have a stronger dissolved capacity to the surrounding rock than low-temperature and low-pressure fluids. Therefore, the salinity of

the former is higher, which also indicates that the charging time of hydrocarbon fluids occurred in the late stage. If oil or gas was charged at an early stage, it was difficult to reveal a good linear relation between the salinity and temperature of the inclusions, as shown in Fig. S7E.

4.2.3 Origin and time of dissolution

Deep hydrothermal solutions, deep burial dissolution, and meteoric water leaching easily form secondary pores in rocks (Baruch et al., 2015; Yuan et al., 2015b; França et al., 2003; Taylor and Land, 1996; Surdam et al., 1984). Coal-measure source rocks commonly decompose plant residues to generate organic acids in the early diagenetic stage, reaching a peak at temperatures of 80–140 °C (middle diagenesis) (Dias et al., 2002; Knauss et al., 1997; Surdam et al., 1989). Acid production in coal-measure strata is usually several times that of other source rocks (Wang Y Q et al., 2020). The J_1h , J_1x and J_1d^{1-3} thick-bedded source rocks in the northern Qaidam Basin are coal-measure strata, which offer rich organic acids through deep faults (Figs. S1 and 5) (Ma et al., 2018; Liu et al., 2017). This was confirmed by inclusions from deeper underground at an HT of 175 °C (Fig. S7G). Well-preserved intergranular dissolved pores (Figs. 5a–5d, 5g–5i and 6) and HCE (Figs. S7F, S7G and 8) imply that the pore spaces are mainly derived from deep dissolution.

The Paleogene, when the PETM occurred, was a greenhouse age marked by warming and CO_2 levels in the atmosphere at least three times as high as the current (Shahzad et al., 2019; Dera et al., 2011; Takashima et al., 2006; Pagani et al., 2005). Therefore, meteoric freshwater with a high concentration of CO_2 penetrated through shallow faults and offered vital acidic fluids for shallow dissolution (Fig. S1). Additionally, the relatively high pore water geochemistry at both 2 000 and 5 000 m also indicates the possible presence of two fluid sources above and below (Fig. 7).

However, deep burial dissolution is obviously superior to shallow dissolution (Guo J J et al., 2018). The main reason is that the reservoirs are buried deeply, and the secondary pores formed by meteoric freshwater leaching and dissolution are not easily preserved (Pan S L et al., 2021). The dissolved carbonate cements (Fig. 5h), relatively late diagenesis and HCE (Figs. S7 and S8) all reveal that the secondary pores of the fine-grained sandstones in the study area are mainly derived from late dissolution.

4.2.4 Geochemical diagenetic system

A single sand body with a relatively thin thickness is beneficial for forming an open diagenetic system. In addition, widely developed deep faults offer the essential conditions for material transfer.

Most intense organic acid dissolution occurs in potential reservoirs with favorable fluid migration pathways (e.g., fractures, unconformities and original pore-seepage pathways) and adjacent to source rocks that produce plenty of organic acids (Yuan et al., 2013; Barth and Bjørlykke, 1993). This interpretation suggests that the dissolved pores, which are roughly consistent with the vertical distribution of microfractures, were more common in the middle part (2 600–3 800 m) than in the upper

or lower part of the Upper Paleogene (Figs. 6d, 6e) (Guo J J et al., 2018; Chen et al., 2012). In addition, surface/meteoric diagenesis reaching a maximum depth of 1 500–2 000 m through fractures occurred in a relatively open geochemical system (Yuan et al., 2015a; Giles and de Boer, 1990). The high flow rates of original lake/meteoric freshwater resulted in significant variations in carbon and oxygen isotopes, deposit composition, and the development of secondary pores during early diagenesis (Wang Y T et al., 2021; Yuan et al., 2017).

The transport ability of individual faults is relatively limited, while multifault fracture zones have effective vertical delivery capacity for pore waters, oil-gas and organic acids (Fig. S1). In deep burial diagenesis, closed geochemical systems are common due to the constraints of pore water flow rates and concentration gradients (Lai et al., 2017; Gluyas et al., 2000). However, concentrated fluid flow within fractures/faults suggests a relatively open system (Bjørlykke and Jahren, 2012).

The origin of pore waters, organic acid dissolution, and abundant deep faults all offer convincing evidence for the open geochemical system formed in the burial process of the Upper Paleogene. The pores (primary and dissolved) yielded more near the basal unconformity or source rocks than at the deeper base (3 600–4 400 m) (Figs. 6b, 6c, 6e). The relative primary porosity climbs up and then declines with decreasing distance from unconformity/source rocks below and increasing depth (Fig. 6f). In the range of 2 600–3 900 m, the relative dissolved porosity in the middle is lower than that at the base (Fig. 6g). The dissolution and reprecipitation of early calcite cements formed anhydrite cements in the absence of water injection, which were close to migration pathways (faults) and organic acids (source rocks) in late diagenesis (Gluyas et al., 1997b). The Ba^{2+} and even SO_4^{2-} required by barite and anhydrite originated from the original lake/meteoric water in an arid climate and the dissolution of clastic grains in potential reservoirs (Table S2). All these results indicated that Upper Paleogene sandstones were in an open diagenetic system. Slight vertical differences in the geochemical features of pore waters, for another, show a relatively open system on the whole. Lateral changes suggest that the fracture systems are asymmetrically distributed in the lateral direction (Fig. 7).

4.3 Diagenetic Stage and Evolutionary Sequence

Petrological evidence (epochal phenomena of calcite and the occurrence of anhydrite) (Fig. 4) and XRD analysis of clay minerals (Table S3) all can be used to interpret the relative diagenetic stages in the study area. In addition, the formation temperatures of authigenic minerals are measured from brine inclusions (Fig. S7) or calculated from oxygen isotopes to deduce a more accurate timing of different diagenesis (Feng et al., 2021; Sun et al., 2015). Combined with the above, it was confirmed that the fine-grained sandstones mainly formed during the early diagenetic B substage to the middle diagenetic A substage according to the current standards of “SY/T5477-2003 Division of Diagenetic Stages in Clastic Rocks” in China’s oil and gas industry (Ying et al., 2003). Based on diagenetic stages and previous studies (Sun et al., 2015; Ying et al., 2003), the diagenetic sequence and porosity evolution of the Upper Paleogene sandstones are presented in Fig. 8.

The diagenetic sequence occurs successively: (1) deposition of many clay matrix and mechanical compaction; (2) precipitation of chlorite rims; (3) precipitation of early calcite and anhydrite cements; (4) dissolution of feldspar, rock fragments, early calcite; (5) precipitation of authigenic clay minerals (smectite and I/S mixed-layer); (6) quartz and feldspar overgrowths; (7) precipitation of late anhydrite; (8) precipitation of pore-filling chlorite/illite; (9) hydrocarbon charging; (10) albitization of plagioclase; (11) precipitation of late calcite cements (ferrocalcite) as replacement of feldspar, late anhydrite and rock fragments (Figs. 4 and 8).

In the Upper Paleogene sandstones, mechanical compaction is common, but chemical compaction is rare (Fig. 4). Acidic fluids often reacted with unstable materials (feldspar, volcanic/metamorphic rock fragments, carbonate, anhydrite) to form pore spaces (Fig. 5). The early diagenetic B substage continues the relatively strong compaction and point contact of the A substage. R_o is 0.4%–0.5%, and the temperature is 65–85 °C. Early calcite cements represent the initial alkaline environment in this stage. Rare siliceous cements and quartz overgrowth indicate a weakly acidic diagenetic environment, and a mixed layer of clay minerals begins to appear (Fig. 8). Intergranular pores are partially filled with calcite cements or clay matrix and dissolved. The primary pore volume decreases with compaction and cementation, while the secondary pore volume increases (Fig. 8).

In the middle diagenetic A substage with relatively weak compaction and point-line contact, ferrocalcite begins to appear, and quartz and feldspar overgrowths increase. R_o is 0.5%–1.0%, and the temperature is 85–130 °C. The replacement of a few late carbonate cements suggests a weakly alkaline environment in this late stage (Fig. 8). I/S mixed-layer, pore-filling chlorite and illite are common. Primary pores are basically fixed, and abundant secondary pores occur, forming a mixed pore combination (Fig. 8). The dissolution of calcite grains and early cements and the precipitation of late anhydrite indicate the action of acidic pore fluids.

Chlorite and illite are altered from kaolinite and smectite, respectively, under alkaline conditions (Pan S L et al., 2021). Low I/S and C/S mixed-layer ratios, low smectite/kaolinite and high illite/chlorite (Table S3) all reflect the alteration of smectite to illite, kaolinite to chlorite and middle-late diagenesis. Wang Y T et al. (2021) calculated the diagenetic temperature of Upper Paleogene strata in the study area of 78–117 °C by oxygen isotopes, and this study measured of 80–136 °C by brine inclusions. All of the above results are consistent with the temperatures of illitization and chloritization (80–143 °C) (Du et al., 2020). Anhydrite has a weakly negative correlation with calcite (Table S2), so the late anhydrite developed at 3 000–4 000 m (~110 °C) may have been formed by the dissolution and reprecipitation of early calcite and anhydrite cements. In addition, high concentrations of Ca^{2+} and SO_4^{2-} in pore water also provided material conditions for the formation of anhydrite (Fig. 7). Plagioclase is the dominant feldspar in Upper Paleogene sandstones, while its dissolved and metasomatic residues are albite (Table S2), indicating that the alteration of plagioclase is mainly anorthite (Qing et al., 2020). In mid-deep burial diagenesis, acidic albite and K-feldspar react with organic acids and are dissolved. The transformation of smectite to illite

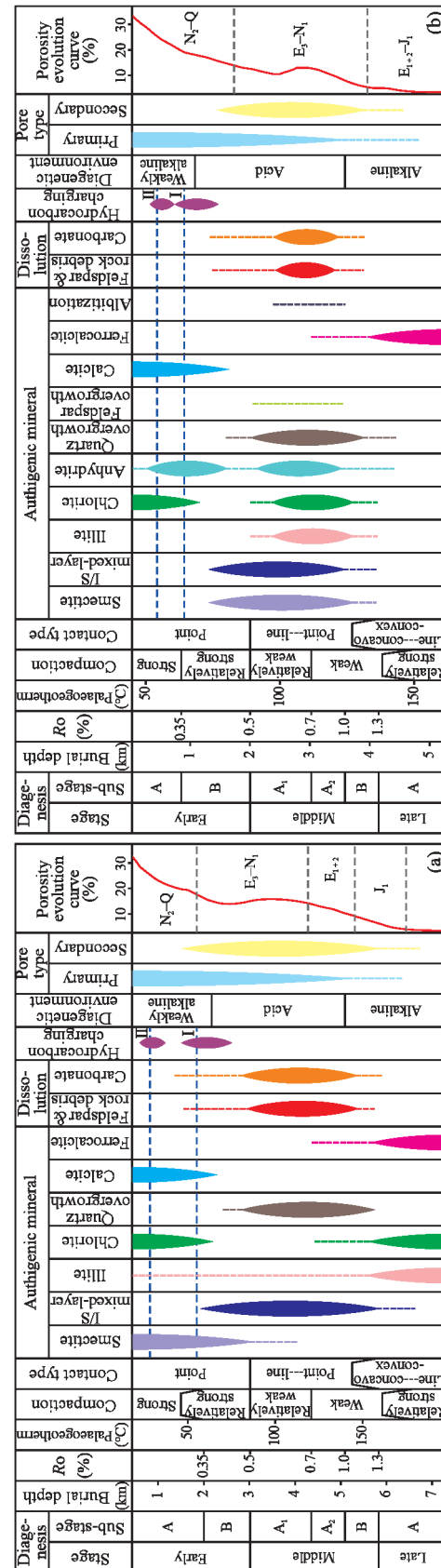


Figure 8. Typical diagenetic sequence and porosity evolution for the Upper Paleogene fine-grained sandstones in the Lenghu (a) and Eboliang (b) tectonic belts.

promotes the dissolution of K-feldspar but inhibits that of albite (Luo et al., 2018). Therefore, the residual feldspar is dominated by albite, and plagioclase albitization occurs.

4.4 Controlling Mechanism and Evaluation Model of High-Quality Reservoirs

4.4.1 Macroscale controlling mechanism

With increasing burial depth, mechanical compaction is the critical and initial factor to reduce pore spaces, especially primary pores (Guo J J et al., 2018; Jia et al., 2013; Chen et al., 2012). Similar to porosity, porosity generally decreases with depth (Figs. 6b and S5A), and primary pores occur mainly in the uppermost Upper Paleogene (Figs. 6c, 6f). Moreover, microfacies also have an important effect on reservoir quality, especially the Upper Paleogene fine-grained sandstones (Fig. 9) (Xie et al., 2022; El-Ghali et al., 2013; Jia et al., 2013). As shown in Fig. 9, ODC, UDC, flood fan and some beach bar or mouth bar sandstones are conducive to the formation of reservoirs. However, the porosity/permeability of different microfacies sandstones usually varies greatly (Gao et al., 2021).

The shallow fault system supplied original lake water seepage and meteoric freshwater leaching for early diagenetic alterations (Fig. S1A) (Wang Y T et al., 2021). Unconformity and deep fault systems were pathways for hydrocarbon migration and acidic fluid flow and played a crucial role in the formation of high-quality reservoirs and open diagenetic systems (Fig. S1A). In summary, basal unconformities, fault systems and open geochemical systems all provided crucial conditions for the formation of whole dissolution. In addition, the first oil-gas charging supplied organic acids for dissolution and pore spaces and pathways for the second oil-gas charging and organic acid flow (Luo et al., 2018). Continuous second oil-gas charging was basically consistent with or slightly later than deep burial dissolution, which was beneficial to the preservation of secondary pores and hydrocarbon accumulation (Figs. 8 and 10) (Chen et al., 2012). Last but not least, the provenance provided rich feldspar, rock fragments, and carbonate as a material base for dissolution and cementation (Yuan et al., 2013).

4.4.2 Microscale controlling mechanism

Porous-type reservoirs composed of primary and residual intergranular pores are the main form of fine-grained sandstones. The reservoir performance of the primary intergranular pores is dominated by argillaceous and micritic contents (Qin

et al., 2022). Residual intergranular pores are affected by diagenesis, clastic grain sorting, sparry calcite content and formation water (Guo J J et al., 2018; Jia et al., 2013).

High-quality Upper Paleogene reservoirs were developed in the ODC sandstones of the delta plain and the UDC sandstones of the delta front. The Ca^{2+} required for early calcite cements filling the pores came from the weathered and dissolved pyroclasts within the provenance and pore waters discharged by compaction. Thus, the diagenetic fluids of adjacent calcareous strata provided crucial Ca^{2+} to the calcite cements in sandstones during the early diagenetic stage (Luo et al., 2018; Fu et al., 2015). The development of low-content calcite and anhydrite cements (<15%) in early diagenesis and the presence of abnormal high-pressure zones reduced the damage of compaction to reservoir pores to some extent. They all played a good role in the protection and support for primary pores, so that these pores were well preserved (Wang Y T et al., 2021; Guo J J et al., 2018).

4.4.3 Evaluation model

Based on microscopic analysis, the early cements and clay matrix are mainly yielded in the periphery of a single sand body but poorly developed in its interior. Hence, the central area of a single sand body is more conducive to the formation of high-quality reservoirs (Fig. 10). The comparison shows that the petrological and mineralogical features of UDC sandstones are basically the same as those of ODC sandstones (Tables S1 and 1). Therefore, their theoretical compaction model and genetic mechanism are extremely similar. Moreover, there were no obvious differences between the two types in diagenetic minerals and sequences.

UDC sandstones in the braided river delta front generally occur in E_3^2 , and their pore spaces are composed of residual primary pores, minor dissolved pores, and fracturing fractures (Figs. S2, 6 and 10). Primary intergranular pores were preserved by abnormally high pressure, chlorite rims, early carbonate cements and some high-content rigid grains in the interior sand body (Table S1 and Fig. 5a, 5d, 5k). However, they were commonly blocked by cementation and compaction near the periphery (Figs. 8 and 10) (Guo J J et al., 2018; Worden and Morad, 2003). Secondary pores were mostly formed by deep burial dissolution of carbonate cements, feldspar and rock fragments in reaction with organic acids and preserved by subsequent charging (Figs. 5a–5i, 6 and 10) (Jia et al., 2013; Yuan et al., 2013). Fault systems are vital migration pathways for acidic fluids and oil-gas (Fig. 10). In addition, the combined action of high concentrations of CO_2 from meteoric freshwater leaching or penetration and thermal decarboxylation of organic matter also provided acidic conditions for dissolution (Wang Y T et al., 2021).

Most shallow dissolved pores were blocked by subsequent cementation and compaction (Figs. 5d, 5h), but many residual dissolved pores, as crucial spaces, are conducive to deep dissolution (Fig. 10). Residual and dissolved primary pores provided migration pathways for the late organic acids from underlying source rocks and accelerated the later dissolution (Luo et al., 2019; Yuan et al., 2013). ODC/UDC sandstones all possess similar compositions, textures and structures, and the

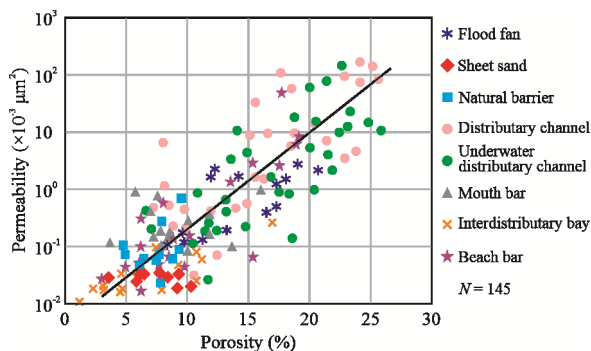


Figure 9. The correlation between porosity and permeability of fine-grained sandstone microfacies.

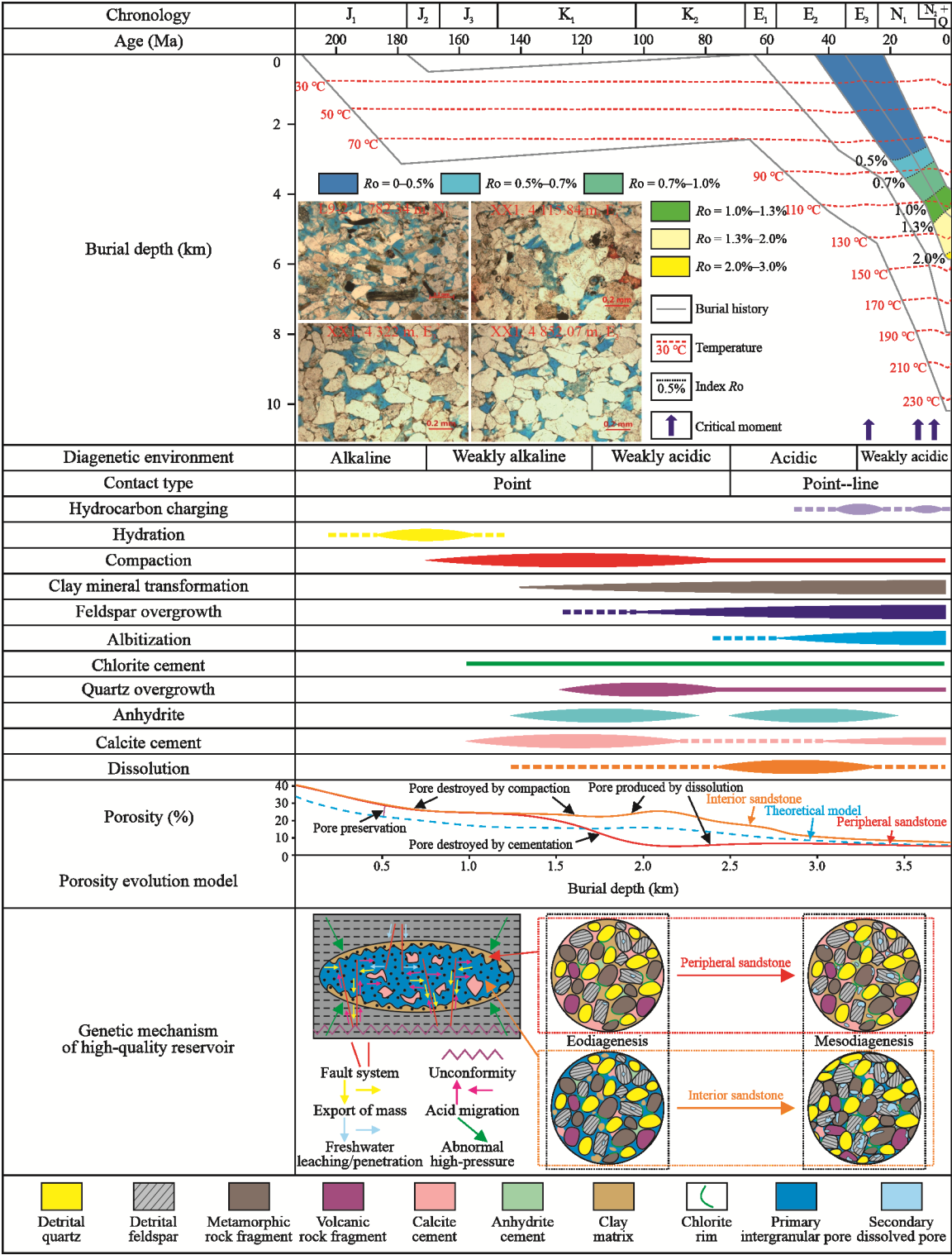


Figure 10. Schematic illustration of the genetic mechanism and porosity evolution of high-quality ODC/UDC sandstone reservoirs.

vertical and lateral occurrences of the overwater part are also similar to or better than those of the underwater part (Tables 1, S1, and Figs. S2, S5). Hence, the genetic mechanism on ODC/UDC sandstones has the optimal conditions to form and develop high-quality reservoirs (Fig. 10).

5 CONCLUSION

(1) Through the correlation analysis of parameters and

permeability, the pore structure in the study area has relatively strong heterogeneity in general, which reflects the features of “small pore-throat, poor sorting, high displacement pressure and poor pore-throat connectivity”. The abrupt increase in the physical properties is mainly due to the abnormally high pressure caused by the undercompaction of thin-bedded sandstone reservoirs developed in a large set of argillaceous rocks. Abnormal pressure zones reduce and inhibit the damage of compac-

tion and overgrowth to reservoir pores, and prolong the dissolved action time of acidic fluids.

(2) The Upper Paleogene pore fluids were mainly derived from original lake water, surface water from rivers/deltas, meteoric water and organic acids from the thermal decarboxylation of organic matter. The acids for the dissolution of unstable materials such as feldspar, metamorphic rock fragments, carbonate, and anhydrite are mainly composed of organic acids that migrated through basal unconformity and deep faults and minor meteoric freshwater with a high concentration of CO_2 that penetrated through the shallow faults.

(3) Surface or meteoric diagenesis of the Upper Paleogene sandstones related to shallow faults occurred in a relatively open geochemical system. The fine-grained sandstones mainly formed during the early diagenetic B substage to the middle diagenetic A substage based on petrological observations, clay mineral analysis, HT of fluid inclusions and isotopic analysis.

(4) Controlling factors of fine-grained sandstone reservoirs in the Upper Paleogene mostly comprise faults, microfacies, burial depth, geothermal field, diagenesis, HCE, and abnormally high pressure. Double fault systems provide the pathways for fluid flow and hydrocarbon migration. The high energy ODC and UDC sandstones are the essential basis. Appropriate burial depth, geothermal field, and HCE represent the vital conditions to retain and increase pore volume. As the main constructive diagenesis, the dissolution of organic acids and meteoric water is conducive to the improvement of reservoir quality. Abnormally high pressure is the key to the formation of high-quality reservoirs. Based on the above, a reservoir model for the ODC/UDC fine-grained sandstones with bidirectional pathways, rich in clay minerals, poor in cements, superimposed dissolution, and abnormally high pressure is established.

ACKNOWLEDGMENTS

We are grateful to the Exploration & Development Research Institute, Qinghai Oilfield Company for providing all relevant samples, data and permission to publish this information. The study was supported by the National Major Science and Technology Projects of China (No. 2016ZX05033-001-002), the National Natural Science Foundation of China (No. 41272155) and the China Scholarship Council. Thanks go to Puyu Liu, Qi Wang, Yang Han and Wenwen Wu for their work on the core study, thin-section analysis and seismic data processing. We acknowledge the reviewers for their critical comments and constructive suggestions, which greatly improved the manuscript. The final publication is available at Springer via <https://doi.org/10.1007/s12583-022-1701-6>.

Electronic Supplementary Materials: Supplementary materials (ESM I Tables S1–S4; ESM II Figs. S1–S7) are available in the online version of this article at <https://doi.org/10.1007/s12583-022-1701-6>.

REFERENCES CITED

Bao, J., Wang, Y. D., Song, C. H., et al., 2017. Cenozoic Sediment Flux in the Qaidam Basin, Northern Tibetan Plateau, and Implications with Regional Tectonics and Climate. *Global and Planetary Change*, 155: 56–69. <https://doi.org/10.1016/j.gloplacha.2017.03.006>

- Barth, T., Bjørlykke, K., 1993. Organic Acids from Source Rock Maturation: Generation Potentials, Transport Mechanisms and Relevance for Mineral Diagenesis. *Applied Geochemistry*, 8(4): 325–337. [https://doi.org/10.1016/0883-2927\(93\)90002-x](https://doi.org/10.1016/0883-2927(93)90002-x)
- Baruch, E. T., Kennedy, M. J., Löhr, S. C., et al., 2015. Feldspar Dissolution-Enhanced Porosity in Paleoproterozoic Shale Reservoir Facies from the Barney Creek Formation (McArthur Basin, Australia). *AAPG Bulletin*, 99(9): 1745–1770. <https://doi.org/10.1306/04061514181>
- Bentley, R. W., 2002. Global Oil & Gas Depletion: An Overview. *Energy Policy*, 30(3): 189–205. [https://doi.org/10.1016/s0301-4215\(01\)00144-6](https://doi.org/10.1016/s0301-4215(01)00144-6)
- Bethke, C. M., Altaner, S. P., 1986. Layer-by-Layer Mechanism of Smectite Illitization and Application to a New Rate Law. *Clays and Clay Minerals*, 34(2): 136–145. <https://doi.org/10.1346/ccmn.1986.0340204>
- Bjørlykke, K., 1993. Fluid Flow in Sedimentary Basins. *Sedimentary Geology*, 86(1/2): 137–158. [https://doi.org/10.1016/0037-0738\(93\)90137-t](https://doi.org/10.1016/0037-0738(93)90137-t)
- Bjørlykke, K., Gran, K., 1994. Salinity Variations in North Sea Formation Waters: Implications for Large-Scale Fluid Movements. *Marine and Petroleum Geology*, 11(1): 5–9. [https://doi.org/10.1016/0264-8172\(94\)90003-5](https://doi.org/10.1016/0264-8172(94)90003-5)
- Bjørlykke, K., Jahren, J., 2012. Open or Closed Geochemical Systems during Diagenesis in Sedimentary Basins: Constraints on Mass Transfer during Diagenesis and the Prediction of Porosity in Sandstone and Carbonate Reservoirs. *AAPG Bulletin*, 96(12): 2193–2214. <https://doi.org/10.1306/04301211139>
- Cai, J. G., Du, J. Z., Chen, Z. W., et al., 2018. Hydrothermal Experiments Reveal the Influence of Organic Matter on Smectite Illitization. *Clays and Clay Minerals*, 66(1): 28–42. <https://doi.org/10.1346/ccmn.2017.064084>
- Cao, J. J., Luo, J. L., Madina, M., et al., 2021. Influence Mechanism of Micro-Heterogeneity on Conglomerate Reservoir Densification: A Case Study of Upper Permian Wutonggou Formation in DN8 Area of Dongdaohazi Sag, Junggar Basin. *Earth Science*, 46(10): 3435–3452. <https://doi.org/10.3799/dqkx.2020.388> (in Chinese with English Abstract)
- Cao, Y. C., Xi, K. L., Zhu, R. K., et al., 2015. Microscopic Pore Throat Characteristics of Tight Sandstone Reservoirs in Fuyu Layer of the Fourth Member of Quantou Formation in Southern Songliao Basin. *Journal of China University of Petroleum (Edition of Natural Science)*, 39(5): 7–17 (in Chinese with English Abstract)
- Chen, J., Zhang, Y. M., Shi, J. A., et al., 2012. Diagenesis of Paleogene-Neogene Sandstone Reservoirs in Lenghu-Maxian Area, Northern Qaidam Basin. *Lithologic Reservoirs*, 24(2): 21–25 (in Chinese with English Abstract)
- Chen, S. Y., Zhang, S., Wang, Y. S., et al., 2016. Lithofacies Types and Reservoirs of Paleogene Fine-Grained Sedimentary Rocks Dongying Sag, Bohai Bay Basin, China. *Petroleum Exploration and Development*, 43(2): 218–229. [https://doi.org/10.1016/s1876-3804\(16\)30025-8](https://doi.org/10.1016/s1876-3804(16)30025-8)
- Dera, G., Brigaud, B., Monna, F., et al., 2011. Climatic Ups and Downs in a Disturbed Jurassic World. *Geology*, 39(3): 215–218. <https://doi.org/10.1130/g31579.1>
- Dias, R. F., Freeman, K. H., Lewan, M. D., et al., 2002. $\delta^{13}\text{C}$ of Low-Molecular-Weight Organic Acids Generated by the Hydrous Pyrolysis of Oil-Prone Source Rocks. *Geochimica et Cosmochimica Acta*, 66(15): 2755–2769. [https://doi.org/10.1016/s0016-7037\(02\)00871-2](https://doi.org/10.1016/s0016-7037(02)00871-2)
- Du, J. Z., Cai, J. G., Chao, Q., et al., 2021. Variations and Geological Significance of Solid Acidity during Smectite Illitization. *Applied Clay Science*, 204: 106035. <https://doi.org/10.1016/j.clay.2021.106035>
- Du, J. Z., Cai, J. G., Chen, Z. W., et al., 2019. A Contrastive Study of Effects of Different Organic Matter on the Smectite Illitization in

- Hydrothermal Experiments. *Applied Clay Science*, 168: 249–259. <https://doi.org/10.1016/j.clay.2018.11.016>
- Du, Y. L., Fang, W. X., Lu, J., 2020. Characteristics of Diagenetic Temperature-Pressure-Oxygen Fugacity of Gabbro-Diabase and Tendency of Geothermal Evolution of Magma Diagenesis in Sareke, Xinjiang. *Acta Petrologica Sinica*, 36(2): 484–508 (in Chinese with English Abstract)
- El-Ghali, M. A. K., El Khoriby, E., Mansurbeg, H., et al., 2013. Distribution of Carbonate Cements within Depositional Facies and Sequence Stratigraphic Framework of Shoreface and Deltaic Arenites, Lower Miocene, the Gulf of Suez Rift, Egypt. *Marine and Petroleum Geology*, 45: 267–280. <https://doi.org/10.1016/j.marpetgeo.2013.04.019>
- El-Ghali, M. A. K., Tajori, K. G., Mansurbeg, H., 2006. The Influence of Transgression and Regression on the Spatial and Temporal Distribution of Diagenetic Kaolin in the Upper Ordovician Glaciogenic Sandstones within a Sequence Stratigraphic Framework, Murzuq Basin, SW Libya. *Journal of Geochemical Exploration*, 89(1/2/3): 87–91. <https://doi.org/10.1016/j.gexplo.2005.11.030>
- Feng, J. L., Cao, J., Hu, K., et al., 2013. Dissolution and Its Impacts on Reservoir Formation in Moderately to Deeply Buried Strata of Mixed Siliciclastic-Carbonate Sediments, Northwestern Qaidam Basin, Northwest China. *Marine and Petroleum Geology*, 39(1): 124–137. <https://doi.org/10.1016/j.marpetgeo.2012.09.002>
- Feng, Y. W., Chen, Y., Zhao, Z. Y., 2021. Migration of Natural Gas Controlled by Faults of Majiagou Formation in Central Ordos Basin: Evidence from Fluid Inclusions. *Earth Science*, 46(10): 3601–3614. <https://doi.org/10.3799/dqkx.2020.384> (in Chinese with English Abstract)
- Folk, R. L., 1980. Petrology of Sedimentary Rocks. Hemphill Publishing Company, Austin. 4–11
- França, A. B., Araújo, L. M., Maynard, J. B., et al., 2003. Secondary Porosity Formed by Deep Meteoric Leaching: Botucatu Eolianite, Southern South America. *AAPG Bulletin*, 87(7): 1073–1082. <https://doi.org/10.1306/02260301071>
- Fu, S. T., Wang, Z. L., Zhang, Y. S., et al., 2015. Origin of Carbonate Cements in Reservoir Rocks and Its Petroleum Geologic Significance: Eboliang Structure Belt, Northern Margin of Qaidam Basin. *Acta Sedimentologica Sinica*, 33(5): 991–999 (in Chinese with English Abstract)
- Gao, D., Hu, M. Y., Li A. P., et al., 2021. High-Frequency Sequence and Microfacies and Their Impacts on Favorable Reservoir of Longwangmiao Formation in Central Sichuan Basin. *Earth Science*, 46(10): 3520–3534. <https://doi.org/10.3799/dqkx.2020.382> (in Chinese with English Abstract)
- Giles, M. R., de Boer, R. B., 1990. Origin and Significance of Redistributive Secondary Porosity. *Marine and Petroleum Geology*, 7(4): 378–397. [https://doi.org/10.1016/0264-8172\(90\)90016-a](https://doi.org/10.1016/0264-8172(90)90016-a)
- Gluyas, J. G., Garland, C. R., Oxtoby, N. H., et al., 2000. Quartz Cement: The Miller's Tale. In: Worden, R. H., Morad, S., eds., *Quartz Cementation in Sandstones*, vol. 29. International Association of Sedimentologists, Blackwell Science, Oxford. 199–219
- Gluyas, J. G., Robinson, A. G., Primmer, T. P., 1997a. Rotliegend Sandstone Diagenesis: A Tale of Two Waters. *Geofluids II*, Belfast. 291–294
- Gluyas, J., Jolley, L., Primmer, T., 1997b. Element Mobility during Diagenesis: Sulphate Cementation of Rotliegend Sandstones, Southern North Sea. *Marine and Petroleum Geology*, 14(7/8): 1001–1011. [https://doi.org/10.1016/S0264-8172\(97\)00038-x](https://doi.org/10.1016/S0264-8172(97)00038-x)
- Guo, J. J., Sun, G. Q., Men, H. J., et al., 2018. Genetic Analysis of Anomalous High Porosity Zones in deeply Buried Reservoirs in the West Part of Northern Edge of Qaidam Basin, NW China. *Acta Sedimentologica Sinica*, 36(4): 777–786 (in Chinese with English Abstract)
- Guo, P., Liu, C. Y., Huang, L., et al., 2017. Genesis of the Late Eocene Bedded Halite in the Qaidam Basin and Its Implication for Paleoclimate in East Asia. *Palaeogeography, Palaeoclimatology, Palaeoecology*, 487: 364–380. <https://doi.org/10.1016/j.palaeo.2017.09.023>
- Guo, P., Liu, C. Y., Yu, M. L., et al., 2018. Paleosalinity Evolution of the Paleogene Perennial Qaidam Lake on the Tibetan Plateau: Climatic vs. Tectonic Control. *International Journal of Earth Sciences*, 107: 1641–1656. <https://doi.org/10.1007/s00531-017-1564-8>
- Harrison, W. J., Summa, L. L., 1991. Paleohydrology of the Gulf of Mexico Basin. *American Journal of Science*, 291(2): 109–176. <https://doi.org/10.2475/ajs.291.2.109>
- Hower, J., Eslinger, E. V., Hower, M. E., et al., 1976. Mechanism of Burial Metamorphism of Argillaceous Sediment: 1. Mineralogical and Chemical Evidence. *Geological Society of America Bulletin*, 87(5): 725–737. [https://doi.org/10.1130/0016-7606\(1976\)87725:mobmoa>2.0.co;2](https://doi.org/10.1130/0016-7606(1976)87725:mobmoa>2.0.co;2)
- Jia, Y. Y., Shi, J. A., Shen, Y. S., et al., 2013. Research of Structural Reservoir in No. 5 Unit of Lenghu Area. *Journal of Southwest Petroleum University (Science & Technology Edition)*, 35(4): 43–50 (in Chinese with English Abstract)
- Jin, Z. J., Zhu, D. Y., Hu, W. X., et al., 2009. Mesogenetic Dissolution of the Middle Ordovician Limestone in the Tahe Oilfield of Tarim Basin, NW China. *Marine and Petroleum Geology*, 26(6): 753–763. <https://doi.org/10.1016/j.marpetgeo.2008.08.005>
- Knauss, K. G., Copenhaver, S. A., Braun, R. L., et al., 1997. Hydrous Pyrolysis of New Albany and Phosphoria Shales: Production Kinetics of Carboxylic Acids and Light Hydrocarbons and Interactions between the Inorganic and Organic Chemical Systems. *Organic Geochemistry*, 27(7/8): 477–496. [https://doi.org/10.1016/s0146-6380\(97\)00081-8](https://doi.org/10.1016/s0146-6380(97)00081-8)
- Lai, J., Wang, G. W., Chai, Y., et al., 2017. Deep Burial Diagenesis and Reservoir Quality Evolution of High-Temperature, High-Pressure Sandstones: Examples from Lower Cretaceous Bashijiqike Formation in Keshen Area, Kuqa Depression, Tarim Basin of China. *AAPG Bulletin*, 101(6): 829–862. <https://doi.org/10.1306/08231614008>
- Li, L. L., Wu, C. D., Fan, C. F., et al., 2017. Carbon and Oxygen Isotopic Constraints on Paleoclimate and Paleoelevation of the Southwestern Qaidam Basin, Northern Tibetan Plateau. *Geoscience Frontiers*, 8(5): 1175–1186. <https://doi.org/10.1016/j.gsf.2016.12.001>
- Li, W. W., Cao, J., Shi, C. H., et al., 2020. Shale Oil in Saline Lacustrine Systems: A Perspective of Complex Lithologies of Fine-Grained Rocks. *Marine and Petroleum Geology*, 116: 104351. <https://doi.org/10.1016/j.marpetgeo.2020.104351>
- Liao, J. H., Wu, K. Q., Er, C., 2022. Deep Reservoir Characteristics and Effective Reservoir Control Factors in Baiyun Sag of Pearl River Mouth Basin. *Earth Science*, 47(7): 2454–2467. <https://doi.org/10.3799/dqkx.2022.017> (in Chinese with English Abstract)
- Liu, X., Zhu, S. F., Du, J. J., et al., 2017. Sedimentary Characteristics of the Jurassic in Western North Margin of Qaidam Basin. *Journal of Palaeogeography*, 19(4): 595–608 (in Chinese with English Abstract)
- Luo, L., Gao, X. Z., Gluyas, J., et al., 2019. Reservoir Quality Prediction of Deeply Buried Tight Sandstones in Extensively Faulted Region: A Case from the Middle–Upper Jurassic Shishugou Group in Central Junggar Basin, NW China. *Journal of Petroleum Science and Engineering*, 175: 22–45. <https://doi.org/10.1016/j.petrol.2018.12.027>
- Luo, L., Gao, X., Meng, W., et al., 2018. The Origin and Alteration of Calcite

- Cement in Tight Sandstones of the Jurassic Shishugou Group, Fukang Sag, Junggar Basin, NW China: Implications for Fluid-Rock Interactions and Porosity Evolution. *Australian Journal of Earth Sciences*, 65(3): 427–445. <https://doi.org/10.1080/08120099.2018.1437773>
- Ma, D. D., Yuan, L., Chen, Y., et al., 2018. Geological Conditions of Natural Gas, Resource Potential and Exploration Direction in the Northern Margin of Qaidam Basin. *Natural Gas Geoscience*, 29(10): 1486–1496 (in Chinese with English Abstract)
- Maast, T. E., Jahren, J., Bjørlykke, K., 2011. Diagenetic Controls on Reservoir Quality in Middle to Upper Jurassic Sandstones in the South Viking Graben, North Sea. *AAPG Bulletin*, 95(11): 1937–1958. <https://doi.org/10.1306/03071110122>
- MacQuaker, J. H. S., Taylor, K. G., Keller, M., et al., 2014. Compositional Controls on Early Diagenetic Pathways in Fine-Grained Sedimentary Rocks: Implications for Predicting Unconventional Reservoir Attributes of Mudstones. *AAPG Bulletin*, 98(3): 587–603. <https://doi.org/10.1306/08201311176>
- Pagani, M., Zachos, J. C., Freeman, K. H., et al., 2005. Marked Decline in Atmospheric Carbon Dioxide Concentrations during the Paleogene. *Science*, 309(5734): 600–603. <https://doi.org/10.1126/science.1110063>
- Pan, S. L., Jiang, Y., Zhu, W. J., et al., 2021. Sedimentary-Diagenetic Characteristics of the Upper Section of the Lower Ganchaigou Formation in Lenghu No. 7 Region, North Qaidam Basin. *Natural Gas Geoscience*, 32(3): 393–404 (in Chinese with English Abstract)
- Pan, Y. S., Huang, Z. L., Li, T. J., et al., 2021. Pore Structure Characteristics and Evaluation of Lacustrine Mixed Fine-Grained Sedimentary Rocks: A Case Study of the Lucaogou Formation in the Malang Sag, Santanghu Basin, Western China. *Journal of Petroleum Science and Engineering*, 201: 108545. <https://doi.org/10.1016/j.petrol.2021.108545>
- Pantopoulos, G., Orita, G. K. L., Armelenti, G., et al., 2021. Depositional Conditions at the Aptian Pre-salt Margins: Evidence from Quantitative Petrography and Textural Analysis of the Mucuri Member, Espirito Santo Basin, Brazil. *Petroleum Geoscience*, 27(4): petgeo2020-112. <https://doi.org/10.1144/petgeo2020-112>
- Peng, J., Zeng, Y., Yang, Y. M., et al., 2022. Discussion on Classification and Naming Scheme of Fine-Grained Sedimentary Rocks. *Petroleum Exploration and Development*, 49(1): 121–132. [https://doi.org/10.1016/s1876-3804\(22\)60009-0](https://doi.org/10.1016/s1876-3804(22)60009-0)
- Qin, S., Shi, W. Z., Wang, R., et al., 2022. Characteristics of Tight Sandstone Reservoirs and Their Controlling Factors of He-1 Member in Hangjinqi Block, Ordos Basin. *Earth Science*, 47(5): 1604–1618. <https://doi.org/10.3799/dqkx.2022.007> (in Chinese with English Abstract)
- Qing, Y. H., Lyu, Z. X., Zhao, F., et al., 2020. Formation Mechanism of Authigenic Laumonites in Tight Sandstone of Member 1 of the Middle Jurassic Shaximiao Formation in the Northeastern Central Sichuan Basin. *Bulletin of Mineralogy Petrology and Geochemistry*, 39(3): 536–547 (in Chinese with English Abstract)
- Ren, C. Q., Gao, X. Z., Zhang, Y. S., et al., 2019. Controlling Factors of Reservoir Quality in Low-Permeability Reservoir within a Sequence Stratigraphic Framework: A Case Study of the Lower Jurassic Sandstones in the Northern Margin of the Qaidam Basin, China. *Australian Journal of Earth Sciences*, 66(4): 589–596. <https://doi.org/10.1080/08120099.2019.1562981>
- Shahzad, K., Betzler, C., Qayyum, F., 2019. Controls on the Paleogene Carbonate Platform Growth under Greenhouse Climate Conditions (Offshore Indus Basin). *Marine and Petroleum Geology*, 101: 519–539. <https://doi.org/10.1016/j.marpetgeo.2018.12.025>
- Song, B. W., Zhang, K. X., Lu, J. F., et al., 2013. The Middle Eocene to Early Miocene Integrated Sedimentary Record in the Qaidam Basin and Its Implications for Paleoclimate and Early Tibetan Plateau Uplift. *Canadian Journal of Earth Sciences*, 50(2): 183–196. <https://doi.org/10.1139/cjes-2012-0048>
- Sun, G. Q., Lü, J. W., Zhao, M. J., et al., 2015. Diagenesis and Sedimentary Environment of Miocene Series in Eboliang III Area. *Acta Sedimentologica Sinica*, 33(2): 337–347 (in Chinese with English Abstract)
- Surdam, R. C., Boese, S. W., Crossey, L. J., 1984. The Chemistry of Secondary Porosity. In: McDonald, D. A., Surdam, R. C., eds., *Clastic Diagenesis*. American Association of Petroleum Geologists. *AAPG Memoir*, 37: 127–149. <https://doi.org/10.1306/m37435c8>
- Surdam, R. C., Crossey, L. J., Hagen, E. S., et al., 1989. Organic-Inorganic Interactions and Sandstone Diagenesis. *AAPG Bulletin*, 73(1): 1–23. <https://doi.org/10.1306/703c9ad7-1707-11d7-8645000102c1865d>
- Takashima, R., Nishi, H., Huber, B., et al., 2006. Greenhouse World and the Mesozoic Ocean. *Oceanography*, 19(4): 82–92. <https://doi.org/10.5670/oceanog.2006.07>
- Taylor, T. R., Land, L., 1996. Association of Allochthonous Waters and Reservoir Enhancement in Deeply Buried Miocene Sandstones: Picaroon Field, Corsair Trend, Offshore Texas. In: Crossey, L. J., Loucks, R., Totten, M. W., eds., *Siliciclastic Diagenesis and Fluid Flow: Concepts and Applications*, vol. 55. SEPM Special Publication, Tulsa. 37–48
- Wang, F., Chen, R., Yu, W., et al., 2021. Characteristics of Lacustrine Deepwater Fine-Grained Lithofacies and Source-Reservoir Combination of Tight Oil in the Triassic Chang 7 Member in Ordos Basin, China. *Journal of Petroleum Science and Engineering*, 202: 108429. <https://doi.org/10.1016/j.petrol.2021.108429>
- Wang, G. W., Chang, X. C., Yin, W., et al., 2017. Impact of Diagenesis on Reservoir Quality and Heterogeneity of the Upper Triassic Chang 8 Tight Oil Sandstones in the Zhenjing Area, Ordos Basin, China. *Marine and Petroleum Geology*, 83: 84–96. <https://doi.org/10.1016/j.marpetgeo.2017.03.008>
- Wang, J. G., Zhang, D. W., Yuan, J. Y., et al., 2019. Characteristics of Reservoir Genesis and Oil-Gas Accumulation in Lacustrine Carbonate in Yingxi Area of Qaidam Basin. *Journal of China University of Mining & Technology*, 48(1): 99–109 (in Chinese with English Abstract)
- Wang, J., Cao, Y. C., Liu, K. Y., et al., 2019. Fractal Characteristics of the Pore Structures of Fine-Grained, Mixed Sedimentary Rocks from the Jimsar Sag, Junggar Basin: Implications for Lacustrine Tight Oil Accumulations. *Journal of Petroleum Science and Engineering*, 182: 106363. <https://doi.org/10.1016/j.petrol.2019.106363>
- Wang, Y. Q., Wang, L., Momohara, A., et al., 2020. The Paleogene Atmospheric CO₂ Concentrations Reconstructed Using Stomatal Analysis of Fossil *Metasequoia* Needles. *Palaeoworld*, 29(4): 744–751. <https://doi.org/10.1016/j.palwor.2020.03.002>
- Wang, Y. T., Sun, G. Q., Zhang, S. C., et al., 2021. Characteristics and Genesis of Carbonate Cement in Abdomen Sandstone in Northern Margin of Qaidam Basin. *Natural Gas Geoscience*, 32(7): 1037–1046 (in Chinese with English Abstract)
- Wang, Z. K., Cao, Y. C., Swennen, R., et al., 2022. Meteoric Freshwater Leaching and Its Significance to Reservoir Quality in a Buried Hill of Lower-Middle Jurassic Fluvial Sandstones: A Case Study from the Huanghua Depression, Bohai Bay Basin, China. *Journal of Petroleum Science and Engineering*, 210: 109834. <https://doi.org/10.1016/j.petrol.2021.109834>
- Wardlaw, N. C., Taylor, R. P., 1976. Mercury Capillary Pressure Curves and the Interpretation of Pore Structure and Capillary Behaviour in

- Reservoir Rocks. *Bulletin of Canadian Petroleum Geology*, 24(2): 225–262. <https://doi.org/10.35767/gscpgbull.24.2.225>
- Worden, R. H., Morad, S., 2003. Clay Mineral Cements in Sandstones. In: Anjos, S. M. C., Deros, L. F., Silva, C. M. A., eds., Chlorite Authigenesis and Porosity Preservation in the Upper Cretaceous Marine Sandstones of the Santos Basin, Offshore Eastern Brazil. Wiley-Blackwell, Oxford. 291–316
- Xie, X. J., Xiong, L. Q., Bai, H. Q., et al., 2022. Characteristics of Favorable Reservoir and Its Distribution Prediction in Middle-Deep Layers in Baiyun Sag, Pearl River Mouth Basin. *Earth Science*, 47(5): 1635–1651. <https://doi.org/10.3799/dqkx.2021.244> (in Chinese with English Abstract)
- Yan, Q., Zhang, Y. F., Fu, H., et al., 2018. High Pressure Mercury Injection and Scanning Electron Microscopy Applied to Characterize Micro- and Nano-Scale Pore Throats in Tight Sandstone Reservoirs: A Case Study of the Fourth Member of Shahejie Formation in Yi176 Block, Zhanhua Sag, Bohai Bay Basin. *Petroleum Geology & Experiment*, 40(2): 280–287 (in Chinese with English Abstract)
- Ye, S. J., Yang, Y. T., Zhang, L., 2021. Characteristics and Distribution of “Sweet Spot” Reservoirs in the Third and Fifth Members of Upper Triassic Xujiahe Formation, Western Sichuan Depression, Sichuan Basin. *Oil & Gas Geology*, 42(4): 829–840 (in Chinese with English Abstract)
- Yin, A., Harrison, T. M., 2000. Geologic Evolution of the Himalayan-Tibetan Orogen. *Annual Review of Earth and Planetary Sciences*, 28: 211–280. <https://doi.org/10.1146/annurev.earth.28.1.211>
- Ying, F. X., He, D. B., Long, Y. M., et al., 2003. Petroleum and Natural Gas Industry Standards of the People’s Republic of China: SY/T5477-2003 The Division of Diagenetic Stages in Clastic Rocks. Petroleum Industry Press, Beijing. 32–41 (in Chinese)
- Yuan, G. H., Cao, Y. C., Gluyas, J., et al., 2015a. Feldspar Dissolution, Authigenic Clays, and Quartz Cements in Open and Closed Sandstone Geochemical Systems during Diagenesis: Typical Examples from Two Sags in Bohai Bay Basin, East China. *AAPG Bulletin*, 99(11): 2121–2154. <https://doi.org/10.1306/07101514004>
- Yuan, G. H., Gluyas, J., Cao, Y. C., et al., 2015b. Diagenesis and Reservoir Quality Evolution of the Eocene Sandstones in the Northern Dongying Sag, Bohai Bay Basin, East China. *Marine and Petroleum Geology*, 62: 77–89. <https://doi.org/10.1016/j.marpetgeo.2015.01.006>
- Yuan, G. H., Cao, Y. C., Yang, T., et al., 2013. Porosity Enhancement Potential through Mineral Dissolution by Organic Acids in the Diagenetic Process of Clastic Reservoir. *Earth Science Frontiers*, 20(5): 207–219 (in Chinese with English Abstract)
- Yuan, G. H., Cao, Y. C., Zhang, Y. C., et al., 2017. Diagenesis and Reservoir Quality of Sandstones with Ancient “Deep” IncurSION of Meteoric Freshwater—An Example in the Nanpu Sag, Bohai Bay Basin, East China. *Marine and Petroleum Geology*, 82: 444–464. <https://doi.org/10.1016/j.marpetgeo.2017.02.027>
- Yuan, J. Y., Huang, C. G., Zhao, F., et al., 2015. Carbon and Oxygen Isotopic Compositions, and Palaeoenvironmental Significance of Saline Lacustrine Dolomite from the Qaidam Basin, Western China. *Journal of Petroleum Science and Engineering*, 135: 596–607. <https://doi.org/10.1016/j.petrol.2015.10.024>
- Zhang, M. M., Li, Z., 2018. The Lithofacies and Reservoir Characteristics of the Fine-Grained Sedimentary Rocks of the Permian Lucaogou Formation at the Northern Foot of Bogda Mountains, Junggar Basin (NW China). *Journal of Petroleum Science and Engineering*, 170: 21–39. <https://doi.org/10.1016/j.petrol.2018.06.007>
- Zhang, P. H., Lee, Y. I., Zhang, J. L., 2020. Diagenetic Controls on the Reservoir Quality of Tight Oil-Bearing Sandstones in the Upper Triassic Yanchang Formation, Ordos Basin, North-Central China. *Journal of Petroleum Geology*, 43(2): 225–244. <https://doi.org/10.1111/jpg.12759>
- Zhang, S. M., Cao, Y. C., Liu, K. Y., et al., 2019. Characterization of Lacustrine Mixed Fine-Grained Sedimentary Rocks Using Coupled Chemostratigraphic-Petrographic Analysis: A Case Study from a Tight Oil Reservoir in the Jimusar Sag, Junggar Basin. *Marine and Petroleum Geology*, 99: 453–472. <https://doi.org/10.1016/j.marpetgeo.2018.10.039>
- Zhang, S. M., Zhang, X. J., Zhang, T. J., et al., 2021. Analysis of the Basic Characteristics and Controlling Factors of Fine-Grained Clastic Rock Reservoirs: A Case Study of the Cenozoic in the Mangya Area, Western Qaidam Basin. *Acta Sedimentologica Sinica*. <https://doi.org/10.14027/j.issn.1000-0550.2021.101> (in Chinese with English Abstract)
- Zhang, W., Jian, X., Fu, L., et al., 2018. Reservoir Characterization and Hydrocarbon Accumulation in Late Cenozoic Lacustrine Mixed Carbonate-Siliciclastic Fine-Grained Deposits of the Northwestern Qaidam Basin, NW China. *Marine and Petroleum Geology*, 98: 675–686. <https://doi.org/10.1016/j.marpetgeo.2018.09.008>
- Zhang, X. L., Gao, Z. Q., Fan, T. L., et al., 2020. Element Geochemical Characteristics, Provenance Attributes, and Paleosedimentary Environment of the Paleogene Strata in the Lenghu Area, Northwestern Qaidam Basin. *Journal of Petroleum Science and Engineering*, 195: 107750. <https://doi.org/10.1016/j.petrol.2020.107750>
- Zhao, J. H., Jin, Z. J., Jin, Z. K., et al., 2017. Mineral Types and Organic Matters of the Ordovician-Silurian Wufeng and Longmaxi Shale in the Sichuan Basin, China: Implications for Pore Systems, Diagenetic Pathways, and Reservoir Quality in Fine-Grained Sedimentary Rocks. *Marine and Petroleum Geology*, 86: 655–674. <https://doi.org/10.1016/j.marpetgeo.2017.06.031>
- Zhu, Q., Qiao, X. Y., Zhang, L., 2020. Application of High Pressure Mercury Injection in Pore-Throat Distribution Characterization and Early Productivity Evaluation in Tight Gas Reservoir. *Rock and Mineral Analysis*, 39(3): 373–383 (in Chinese with English Abstract)
- Zou, N. N., Zhang, D. Q., Long, G. H., et al., 2015. Sedimentary System Evolution of Tertiary Reservoirs in Northern Qaidam Basin, China. *Journal of Chengdu University of Technology (Science & Technology Edition)*, 42(2): 149–158 (in Chinese with English Abstract)